

# Chapter 4

## Results and Discussion

"It is a magnificent feeling to recognize the unity of complex phenomena which appear to be things quite apart from the direct visible truth."

Albert Einstein

The present chapter presents the experimental and theoretical results obtained during the work for this thesis.

Section 4.1 focuses on the investigation of sulfur ionization and fragmentation by making use of highly charged ion beams and synchrotron radiation. The spectra were recorded with the help of the two spectrometers already introduced in Chapter 3.3.

Section 4.2, presents experimental results on inner-shell excitation and fragmentation of selenium aggregates, as well as the theoretically calculated fits to the experimental data.

### 4.1 Sulfur Cluster Investigation using HCI beams

As already mentioned in Chapter 2, sulfur vapor consists of a mixture of  $S_n$  clusters, with  $2 \leq n \leq 8$ , the ratios of the aggregates varying with the temperature of the vapor [11, 19]. The ionization energies for the different cluster sizes are known to be found in the energy interval between 8.60 eV and 9.68 eV [109] as shown in Table 4.1.

For comparison reasons, Tab. 4.1 contains also the appearance potentials obtained by electron impact [110]. These are constantly about 0.5 – 0.6 eV higher than the photoionization results, difference considered as being reasonable, as experimentally proven earlier [111].

The interaction of a cluster with a high energy photon, a highly charged ion beam or a highly energetic electron beam can lead to multiple ionization of the cluster. The ion thus formed will

Cluster	Photoionization (eV)	Electron impact (eV)
$S_2^+$	$9.36 \pm 0.02$	$9.9 \pm 0.3$
$S_3^+$	$9.68 \pm 0.03$	$10.5 \pm 0.3$
$S_4^+$	–	$10.4 \pm 0.3$
$S_5^+$	$8.60 \pm 0.05$	$9.9 \pm 0.3$
$S_6^+$	$9.00 \pm 0.03$	$9.8 \pm 0.3$
$S_7^+$	$8.67 \pm 0.03$	$9.3 \pm 0.3$
$S_8^+$	$9.04 \pm 0.03$	$9.6 \pm 0.3$

**Tab. 4.1:** Ionization potentials of sulfur clusters represented as a function of the size of the cluster, as reported in [109] and [110]

tend to electronically relax via various pathways, like the Auger decay, in the case of core excited clusters, which can lead to multiply charged clusters. The interaction with highly charged ion beams can also lead, depending on the charge of the ion beam, to multiply charged clusters. Due to Coulomb repulsion, the doubly or multiply charged clusters will fragment, resulting most often in singly charged fragments. The dissociation can be considered as being instantaneous, while the time-of-flight of the ions in a mass spectrometer are on the microsecond time scale.

When performing a mass spectrometrical investigation one usually uses a time-of-flight mass spectrometer where the extraction of the ions is done in a pulsed mode. As a complementary method, one can make use of a continuous extraction of the ions from the ionization region of the time-of-flight mass spectrometer. One has then the possibility of starting the measurements with the first arriving electron or ion, thus making use of a coincidence technique.

The Photoelectron-photoion-photoion-coincidence (PEPIPICO) technique is based on measuring the arrival time of two correlated ions. From the contour of the correlation plot  $t_2$  vs  $t_1$ , where  $t_1$  is the arrival time of the first ion and  $t_2$  is the arrival time of the first ion, one can extract valuable information about the fragmentation dynamics of the process leading to this cation pair [112]. Previous investigations of the fragmentation of sulfur clusters through ionization via electron impact have been conducted in the mid 1960's [19, 113].

These experiments have concluded that the bigger sulfur aggregates (namely  $S_8$ ,  $S_7$  and  $S_6$ ) fragment for electron energies between 70 and 75 eV.

Proofs of the fragmentation of sulfur clusters ( $S_8$  and  $S_6$ ) have been presented also in other publications as a result of photoionization [109]. No report was found, though, in the literature which would refer to the investigation of sulfur clusters by making use of highly charged ion beams. This makes sulfur clusters an interesting system for the investigations conducted in the present work.

Figures 4.1 and 4.2 present the  $t_2$  vs  $t_1$  correlation plot of sulfur cations recorded after collisions

with  $Xe^{5+}$  and  $Xe^{20+}$  ions, respectively. This allows one to identify the resultant coincident fragmentation channels. The starting signal ( $t = 0$ ) is given by the deflecting pulse applied on the ion beam chopper (see Chapter 3 for details). The measured coincidence signals represent the intensity integral over a two dimensional time window of  $8 \text{ ns} \times 8 \text{ ns}$ .

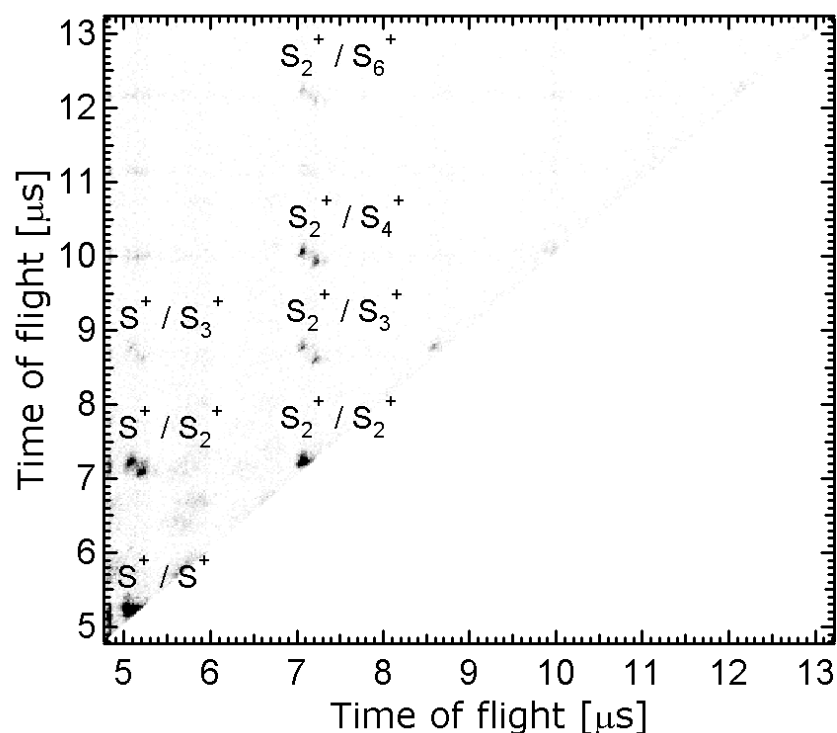


**Fig. 4.1:** Ion-ion-coincidence spectrum of sulfur clusters recorded after ionization with a  $Xe^{5+}$  ion beam

During the coincidence experiments performed, the vapor temperature was kept constant at 400 K, thus allowing us to keep the size distribution of the sulfur aggregates constant (mainly  $S_8$ ). The fragmentation channels identified for the two ion beams are summarized below in Tab. 4.2. It is notable that for the vapor temperature of  $T = 400 \text{ K}$ , the neutral  $S_2$ ,  $S_3$  and  $S_4$  species occur only with a low intensity [19]. This enables us to conclude that the small ionic species we recorded appear from the fragmentation of the dominant aggregate in the vapor, namely  $S_8$ .

$Xe^{5+}$	$S_2^+/S_6^+$	$S_2^+/S_4^+$	$S_2^+/S_3^+$	$S^+/S_2^+$	$S^+/S_3^+$	$S_2^+/S_2^+$	$S^+/S^+$
$Xe^{20+}$	$S_2^+/S_6^+$	$S_2^+/S_4^+$	$S_2^+/S_3^+$	$S^+/S_2^+$		$S_2^+/S_2^+$	$S^+/S^+$

**Tab. 4.2:** Cation pairs identified after ionization with ions beams of  $Xe^{5+}$  and  $Xe^{20+}$ , respectively

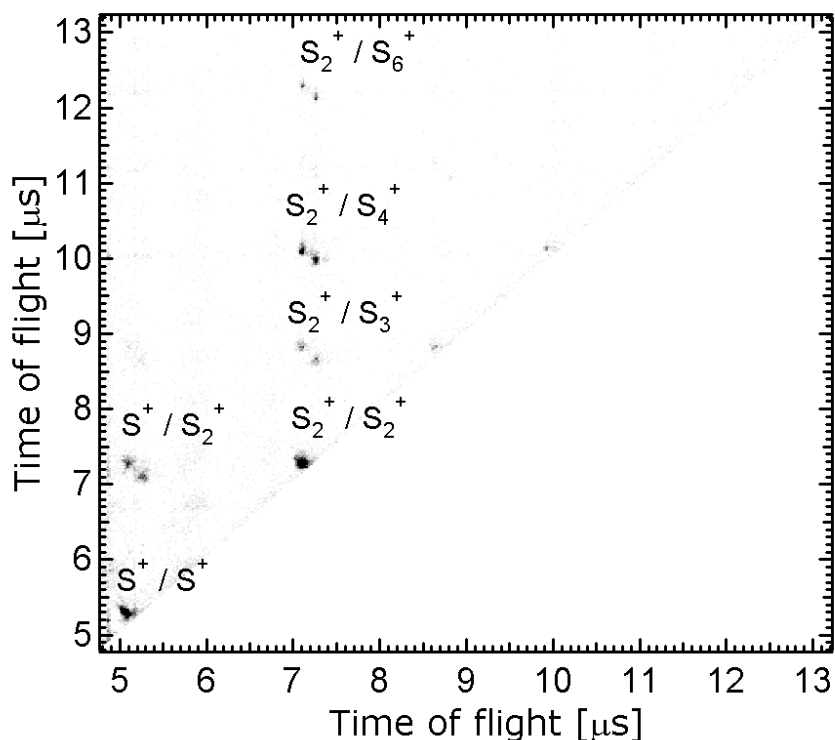


**Fig. 4.2:** Ion-ion-coincidence spectrum of sulfur clusters recorded after ionization with  $Xe^{20+}$  ion beam

An important aspect to take into consideration is that for some of the ion pairs detected, the doubly charged parent ion seems to be  $S_6^{++}$  or even  $S_7^{++}$ . Due to the distribution of the sulfur cluster species in the vapor at 400 K it is sensible to consider that the real parent ion is in fact  $S_8^{++}$ . This leads us to conclude that the original doubly charged ion is releasing a neutral before the charge separation process. More specific statements about the fragmentation dynamics of sulfur cluster requires a more detailed analysis of the coincidence correlation plots. This will be presented in Chapter 4.1.2.

We can conclude that for both the highest and the lowest charge of the ion beam used, we are dealing with various fragmentation processes which lead mostly to the appearance of small cluster fragments.

### 4.1.1 Mass Spectrometry

#### Mass spectrometry as a function of the temperature of the vapor

The mass spectra presented in Figure 4.3 were recorded by making use of photons with a constant energy of  $h\nu = 21.2 \text{ eV}$ .

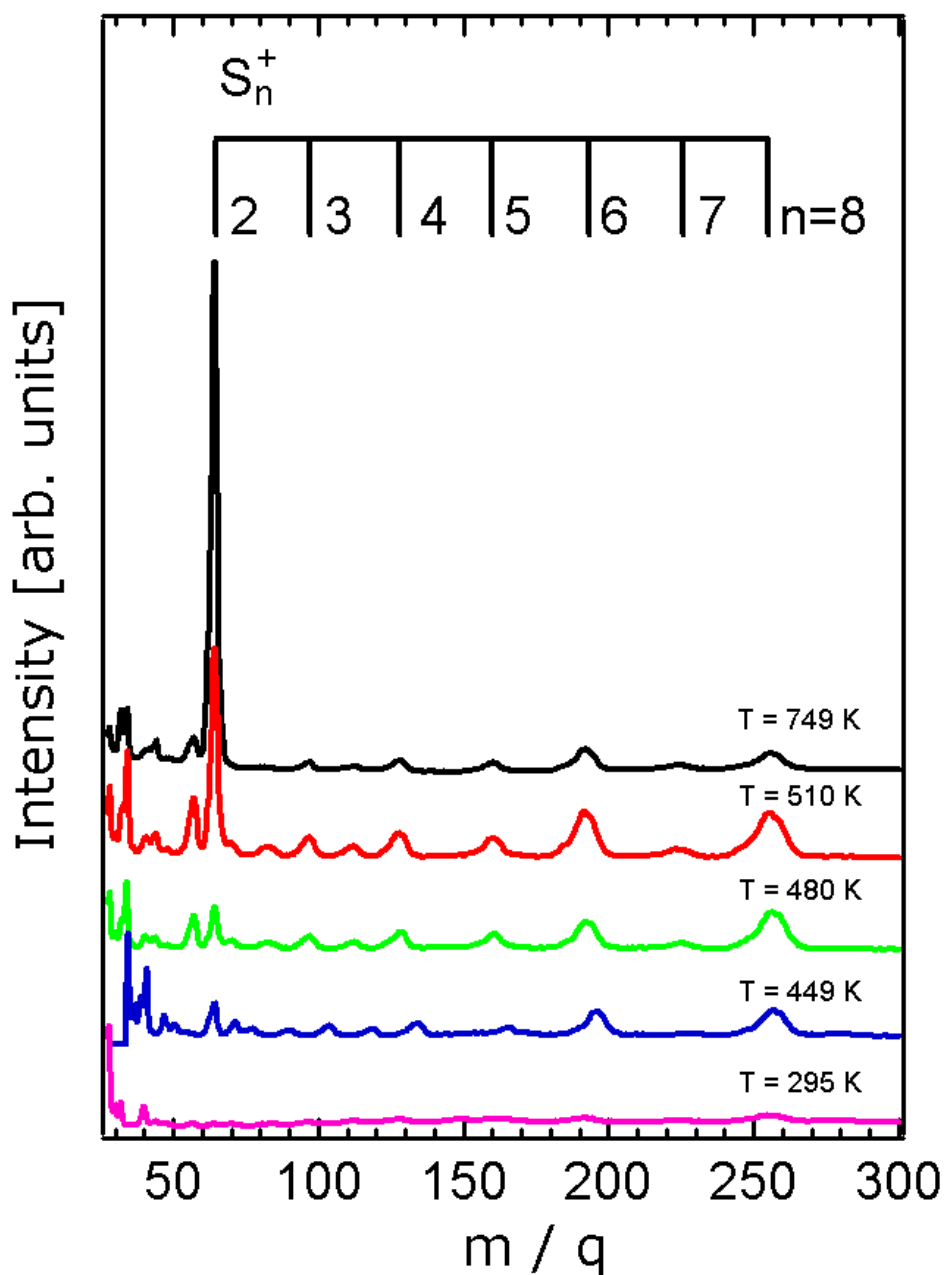


**Fig. 4.3:** Time of flight mass spectra of sulfur vapor after ionization with  $h\nu = 21.2$  eV photons

This energy is above the first ionization energy of sulfur, (see Figure 4.1). The measurements were performed at different temperatures in order to investigate the composition of sulfur vapor as a function of the temperature. The spectrum recorded at  $T = 295$  K is the mass spectrum of the residual gas at a pressure of  $5.1 \times 10^{-6}$  mbar. The dominant peaks in the background spectrum are the ones corresponding to  $m/q = 28$  and  $m/q = 40$  ( $N_2^+$  and  $Ar^+$ , respectively, both components

of the residual gas).

On increasing the temperature of sulfur vapor, the pressure in the chamber increases reaching  $8.8 \times 10^{-6}$  mbar at  $T = 749$  K. Important to notice is that the temperature of the evaporation stage of the oven (see Chapter 3.2.1 for details about the oven source) was kept constant at the temperature of  $438 \pm 3$  K, which is above the melting temperature of sulfur ( $T = 392.6$  K).

At  $T = 449$  K and  $T = 480$  K, one can observe that the dominant peaks are the ones corresponding to  $m/q = 256$  ( $S_8^+$ ) and  $m/q = 192$  ( $S_6^+$ ). At  $T = 510$  K, on the other hand, the most prominent mass signal is the one for  $m/q = 64$ , attributed to  $S_2^+$ , the intensity of this peak increasing further for  $T = 749$  K.

Notable is that up to  $T = 749$  K we do not observe the appearance of atomic sulfur which is in agreement with previous work on sulfur [114]. According to Berkowitz and Marquart [19], sulfur vapor should be monoatomic at  $T = 2500$  K.

The variation in the intensity of the sulfur cluster species with temperature is summarized in Tab. 4.3. The mass peaks are normalized to the intensity of the  $S_8^+$  peak.

Temperature [K]	$S_2^+$	$S_3^+$	$S_4^+$	$S_5^+$	$S_6^+$	$S_7^+$	$S_8^+$
295	0.28	0.35	0.55	0.77	0.77	0.68	1
449	0.59	0.37	0.48	0.32	0.77	0.22	1
480	0.61	0.35	0.45	0.44	0.73	0.27	1
510	1.97	0.44	0.50	0.45	0.91	0.26	1
749	7.31	0.46	0.48	0.48	0.91	0.46	1

**Tab. 4.3:** Mass peaks' intensities normalized to the intensity of the  $S_8^+$  mass peak, as recorded after ionization with  $h\nu = 21.2$  eV photons at different temperatures of selenium vapor, as shown in Fig. 4.3

## Mass spectrometry as a function of the ionization energy

Mass spectra were recorded after ionization of the sulfur vapor with various  $Xe^{q+}$  ion beam charges, ranging from  $q = 2$  up to  $q = 20$ . The Xe ions were accelerated at potentials of 10 kV, the only exception being the  $Xe^{15+}$  where the acceleration potential was set at 8 kV. The respective recorded mass spectra are presented in Fig. 4.4. During the measurements, the temperature of the heating stage of the oven was kept constant at  $T = 405 \pm 3$  K. This yielded a pressure in the interaction chamber of  $2.9(\pm 0.2) \times 10^{-6}$  mbar, whereas the base pressure was  $9.7 \times 10^{-7}$  mbar.

One can observe that for small charges of the ion beam ( $Xe^{2+}$ ), the mass spectra is dominated by singly charged sulfur ions, like  $S_3^+$ ,  $S_2^+$  and  $S^+$ . Considering the composition of neutral sulfur vapor [19], it is clear according to the previous section to assume that these ions are fragments resulting from the dissociation of bigger sulfur clusters, like  $S_8$ .

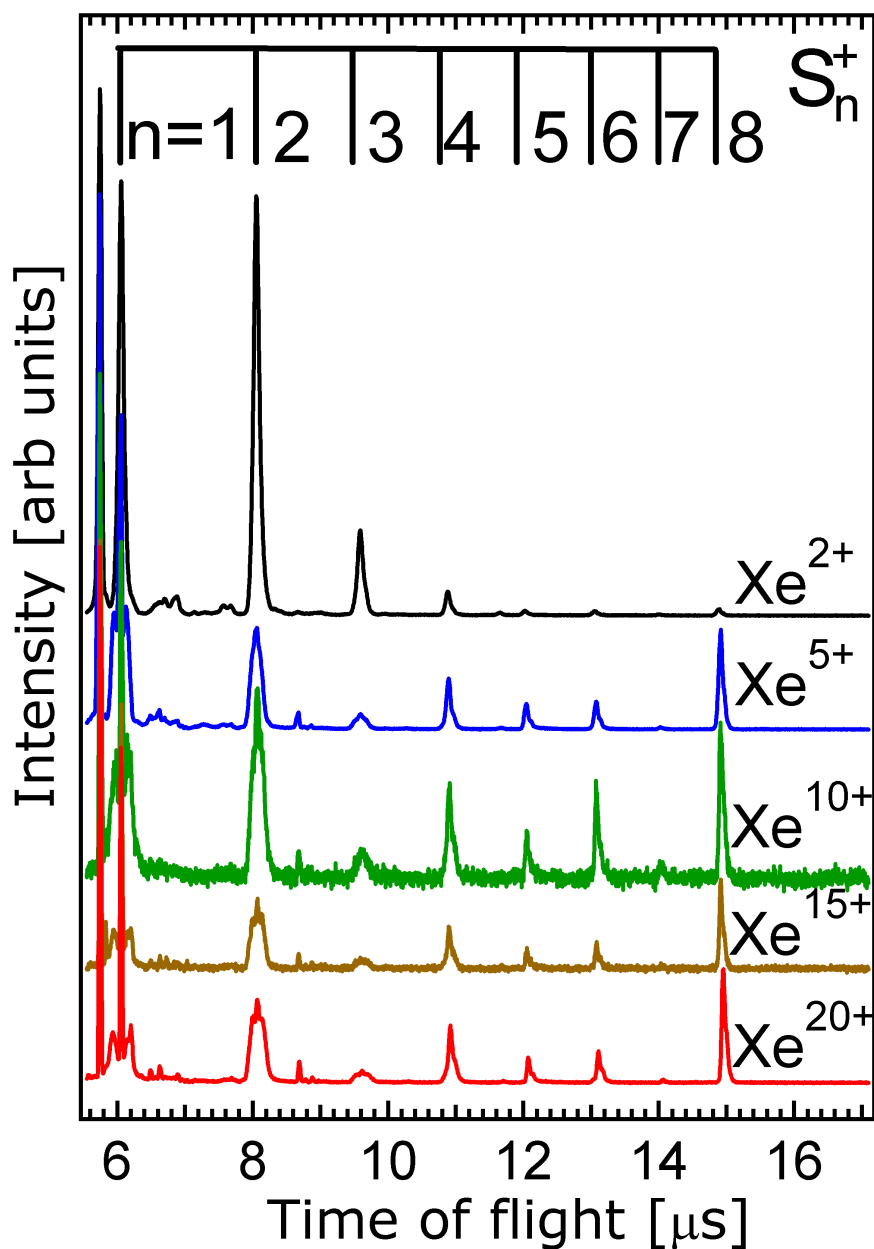


**Fig. 4.4:** Time of flight mass spectra of sulfur clusters recorded after ionization with various  $Xe^{n+}$  ion beam charges

The intensity of the molecular fragments decreases with increasing charge state of the projectile. This implies that fission becomes the dominant process leading to the formation of correlated fragment ions of considerable kinetic energy. Evidence for this assumption will be given in the following section in the context of ion-ion-coincidence experiments.

The variation in the intensity of the sulfur cluster species with the charge of the highly charged

ion beam as presented in Fig. 4.4 is summarized in Tab. 4.4. The mass peaks are normalized to the intensity of the  $S_8^+$  peak.

Ionic Species	$Xe^{2+}$	$Xe^{5+}$	$Xe^{10+}$	$Xe^{15+}$	$Xe^{20+}$
$S_8^+$	1	1	1	1	1
$S_7^+$	0.37	0.04	0.31	0.11	0.03
$S_6^+$	0.91	0.33	0.65	0.50	0.36
$S_5^+$	1.02	0.31	0.39	0.42	0.25
$S_4^+$	3.34	0.65	0.93	0.87	0.75
$S_3^+$	12.75	0.36	0.83	0.79	0.38
$S_2^+$	56.80	2.19	2.73	2.16	2.02
$S^+$	53.24	4.75	3.15	1.12	1.46

**Tab. 4.4:** Mass peaks' intensities normalized to the intensity of the  $S_8^+$  mass peak, as recorded after ionization with ionization with various  $Xe^{n+}$  ion beam charges, as shown in Fig. 4.4

As part of the  $m/q = 32$  peak, characteristic wings are observable, which are due to particularly energetic ions, resulting from fission processes. The wings are getting more pronounced with increasing projectile charge state  $q$ , being almost absent for  $q = 5$  and very pronounced for  $q = 20$ .

In contrast, the neighboring particularly sharp mass line is due to the residual molecular nitrogen parent ion which is formed without kinetic energy release. This implies that for the  $m/q = 32$  peak, mostly the wings are due to  $S^+$  fragments, whereas the central part of the mass signal is preferably due to  $O^{2+}$  from the residual gas. A similar change in peak shape with increasing projectile charge  $q$  is observed for the  $S^{2+}$  signal, where also wings of high kinetic energy ions are observed (see Fig. 4.4), pointing to fission as the origin of this product ion.

In addition, there is evidence for light ions in the mass spectra obtained after HCI impact (as it can be seen in Fig. 4.5). These are assigned to be mostly due to multiply charged oxygen, which comes from the fragmentation of water molecules from the residual gas [115, 116]. This assignment is supported by intense mass signals of water and its fragments.

It cannot be fully excluded that there are also minor contributions from highly charged sulfur ions since the  $S/O$ -mass ratio is 2. However, also in the coincidence mass spectra there is no visible evidence for correlated fragments involving highly charged sulfur ions.

Another point that serves to discount the occurrence of highly charged sulfur ions is the fact that both odd and even sulfur species should occur, similar to earlier work on rare gas clusters [8, 117]. There, it was found that a series of multiply charged atomic fragments occurs as a result of cluster fragmentation. This result was explained in terms of charge localization [8], which evidently does

not occur in the case of sulfur clusters.

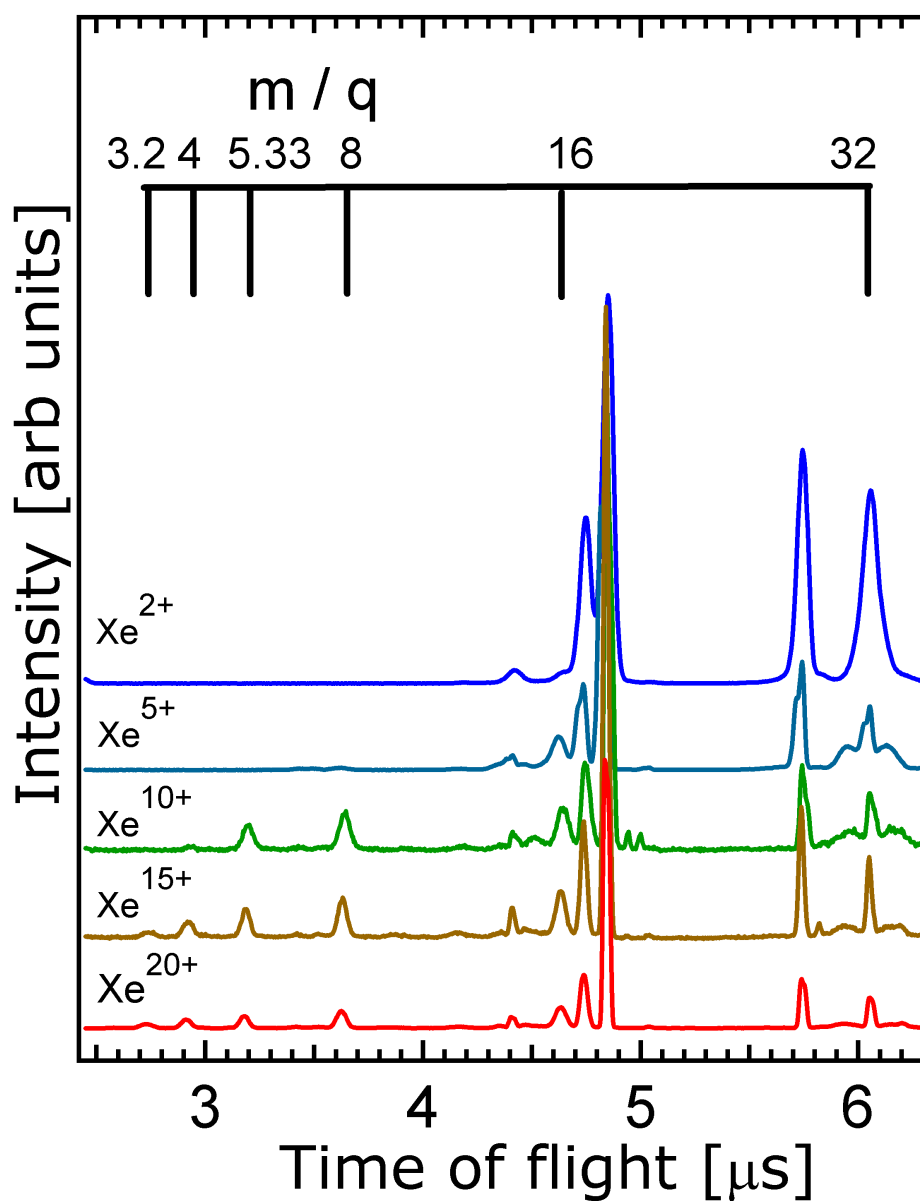


**Fig. 4.5:** Time of flight mass spectra of sulfur clusters recorded after ionization with various  $Xe^{n+}$  ion beam charges

However, as it can be seen in Fig. 4.5 only ions with  $m/q = 16$ ,  $m/q = 8$ ,  $m/q = 5.33$ ,  $m/q = 4$  and  $m/q = 3.2$  are observed. These  $m/q$  ratios would correspond only to even sulfur ions or odd and even oxygen ions. This enables to conclude that these peaks correspond actually to oxygen ions.

## 4.1.2 Ion-ion-coincidence Spectroscopy

The ion-ion-coincidence spectroscopy technique has been employed for investigating the fragmentation of sulfur clusters after ionization with highly charged ion beams. From the analysis of the time of flight distribution of the cations recorded in coincidence in a two-dimensional plot ( $t_2$  vs  $t_1$ , where  $t_2$  is the arrival time of the second cation and  $t_1$  is the flight time of the second negatively charged ion) one can draw important conclusions regarding the dynamics of the fragmentation process involved in the occurrence of the ion pairs. The fragmentation of clusters can take place in one or more steps, each different process being visible through a different correlation plot pattern. Thus it is possible to differentiate between two-, three- or four-body fragmentation processes.

Throughout the ion-ion-coincidence experiments we have used ion beams of  $Xe^{n+}$ , with  $n = 5, 10, 15, 20$ , accelerated at potentials of  $10\text{ kV}$  (for  $n = 5, 10, 20$ ) and  $8\text{ kV}$  (for  $n = 15$ ).

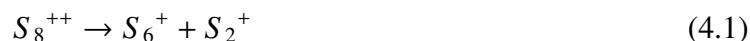
### 4.1.2.1 $Xe^{5+}$ ion beam

Figure 4.6 shows the correlation plots of the coincidence signals recorded after ionizing sulfur clusters with an ion beam of  $Xe^{5+}$  accelerated at  $10\text{ kV}$ . The cation pairs identified were:  $S_2^+/S_6^+$ ,  $S_2^+/S_4^+$ ,  $S_2^+/S_3^+$ ,  $S^+/S^{2+}$ ,  $S^+/S^{3+}$ ,  $S_2^+/S_2^+$  and  $S^+/S^+$ , as seen in Fig.4.1.

The temperature of the second stage of the cluster source (see Chapter 3.2.1 for more details about the experimental setup) was kept constant at  $T = 400\text{ K}$  during the measurements, thus allowing us to keep the size distribution of the sulfur aggregates constant (mainly  $S_8$ ).

#### $S_2^+/S_6^+$

In the case of the  $S_2^+/S_6^+$  cation pair (see Fig.4.6 (a)), the experimental slope of the correlation plot is determined to be  $m = -1.0 \pm 0.1$ . This slope is interpreted as an indication of a *two-body dissociation* mechanism [66] originating from  $S_8^{++}$ , as described by the process:



The kinetic energy release (*KER*) accompanying this fragmentation process is  $3.2 \pm 0.8\text{ eV}$  which corresponds to a charge separation distance (*CSD*) of  $4.5 \pm 0.9\text{ \AA}$ . This result is likely to indicate a charge separation where the charges are located at almost opposite sites (e. g. atoms 1 and 4, in Fig. 4.7) in the  $S_8$  cluster, where the bond length is slightly increased as a result of the double

ionization. This conclusion was drawn considering that the  $S - S$  bond length in  $S_8$  is  $2.055 \text{ \AA}$  [118, 119, 120].

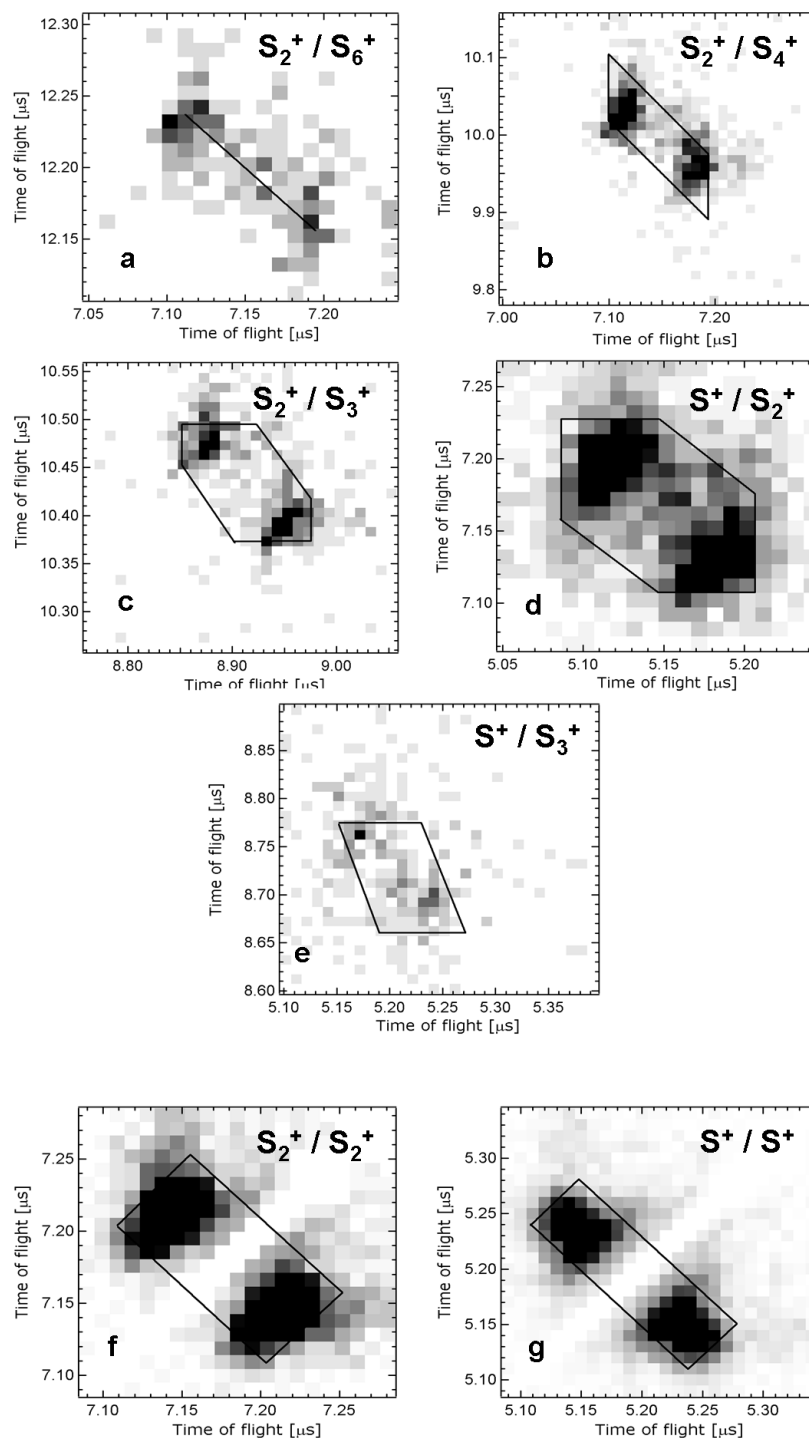


**Fig. 4.6:** Ion-ion-coincidence correlation plots of sulfur aggregates ionized via collisions with  $Xe^{5+}$  ions

**S<sub>2</sub><sup>+</sup>/S<sub>4</sub><sup>+</sup>**

For the S<sub>2</sub><sup>+</sup>/S<sub>4</sub><sup>+</sup> cation pair (see Fig.4.6 (b)), the experimentally obtained slope is  $m = -1.6 \pm 0.1$ . This suggests that the process leading to the occurring of this correlation plot is a secondary decay 4.2 involving the lighter cation, as described by:



The charge separation process is accompanied by the release of  $3.8 \pm 0.7$  eV, which corresponds to a charge separation distance prior to the fission of  $3.8 \pm 0.6$  Å. This charge separation distance suggests a localization of the charges at second neighboring sites in the cluster (e. g. at atoms 1 and 3 in Fig. 4.7) before the charge separation step. The loss of the neutral moiety is accompanied by a considerably smaller kinetic energy release, namely  $2.7 \pm 0.8$  eV.

**S<sub>2</sub><sup>+</sup>/S<sub>3</sub><sup>+</sup>**

For this cation pair (see Fig.4.6 (c)), the experimental slope obtained is  $m = -1.5 \pm 0.2$ . The mechanism proposed for the explanation of the experimental slope of the ion-ion-coincidence signal is a secondary decay in competition described by 4.3:



The kinetic energy released during the charge separation step equals to  $1.7 \pm 0.3$  eV. From this value, the charge separation distance was inferred to have been  $8.5 \pm 1.8$  Å prior to fission. Such a small charge separation distance is a clear indication of the two charges being localized at opposite sites in the parent cluster (e. g. atoms 1 and 5 in Fig. 4.7). The loss of neutral moieties is accompanied by a kinetic energy release comparable to the other fission processes, namely  $1.8 \pm 0.6$  eV for the release of the S<sub>2</sub> neutral and  $0.8 \pm 0.4$  eV for the loss of the S atom.

**S<sup>+</sup>/S<sub>2</sub><sup>+</sup>**

The calculated slope of this correlation plot (see Fig.4.6 (d)) was determined to be  $m = -1.2 \pm 0.2$ .

This suggests that this cation pair appears as a result of a secondary decay in competition of  $S_8^{++}$ , as depicted bellow:



During the charge separation step of the fission, an kinetic energy of  $2.4 \pm 0.7$  eV is released from the fragment ions, corresponding to a charge separation distance of  $6.0 \pm 1.4$  Å before the fission. The CSD indicates that prior to the charge separation step, the charges were located at opposite sites in the parent cluster (e. g. atoms 1 and 5 in Fig. 4.7). The loss of neutral moieties is accompanied by a notably smaller kinetic energy release, namely  $1.1 \pm 0.4$  eV for the release of the  $S_3$  neutral and  $1.4 \pm 0.6$  eV for the loss of  $S_2$ .

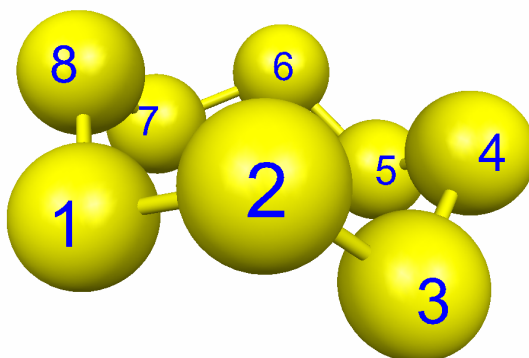


**Fig. 4.7:** The puckered ring structure of the  $S_8$  cluster

### $S^+/S_3^+$

The experimental slope obtained for this correlation plot of the  $S^+/S_3^+$  ion pair (see Fig.4.6 (e)) is determined to be  $m = -3.0 \pm 0.3$ . A plausible fragmentation mechanism explaining the experimental slope which would lead to the appearance of this cation pair is described bellow:



Considering the composition of the neutral sulfur vapor [19], it is considered that the parent ion,  $S_6^{++}$ , originates from  $S_8^{++}$  through the release of a neutral  $S_2$ . The kinetic energy release that accompanies the charge separation process is  $2.4 \pm 0.5$  eV, which corresponds to a charge separation distance prior to the dissociation of  $6.0 \pm 1.0$  Å (charges located at opposite sites in the parent cluster). The release of the neutral  $S_2$  takes place also with a kinetic energy release far smaller than the charge separation stage of the fission of the molecule. The calculated kinetic energy released in the second step of the process described by 4.5 is  $3.6 \pm 1.0$  eV.

### $S_2^+/S_2^+$

For the  $S_2^+/S_2^+$  ion pair (see Fig.4.6 (f)), the experimental slopes of the correlation plot determined to be  $m = -1.0 \pm 0.1$  and  $\beta = 1.0 \pm 0.2$ . This suggests as the occurrence path of this cation pair a two body dissociation process, starting from  $S_4^{++}$ . Considering that in the sulfur vapor the concentration of neutral tetramer is quite low, it was concluded that the parent ion for the  $S_2^+/S_2^+$  pair is a fragment resulting from the decay of  $S_8^{++}$ . This conclusion is also supported by the fact that the slope of the short edges of the correlation plot equals 1. Thus, this correlation plot is the result of a deferred charge separation mechanism, as described by:



During the second step of the dissociation, a kinetic energy of  $3.4 \pm 0.8$  eV is released from the ionic fragments, corresponding to a charge separation distance of  $4.2 \pm 0.8$  Å before fission (equivalent to the charges being located at almost opposite positions, e. g. atoms 1 and 4 in Fig.4.7).

The calculated kinetic energy release in the first step of the process accompanying the release of the neutral  $S_4$  is  $1.7 \pm 0.5$  eV.

### $S^+/S^+$

For the  $S^+/S^+$  ion pair (see Fig.4.6 (g)), the correlation plot consists of a parallelogram with the slope of the longest edge of  $m = -1.0 \pm 0.1$ . At  $T = 400K$ , the used temperature of the vapor during the experiment,  $S_8$  is the major component in the gas phase [19]. It is considered therefore unlikely that the  $S^+/S^+$  ion pair occurs from the two-body dissociation of  $S_2^{++}$ , but instead, from the dissociation of  $S_8^{++}$ , via a deferred charge separation mechanism. This conclusion was drawn considering also that the secondary slope of the parallelogram is  $\beta = 1.0 \pm 0.2$ . Therefore, the proposed mechanism would be:

Ion pair	Edge length (ns)	Edge slope	Proposed mechanism	KER (eV)	CSD (Å)
$S_2^+/S_6^+$	$113 \pm 14$	$m = -1.0 \pm 0.1$	$S_8^{++} \rightarrow S_2^+ + S_6^+$	$3.2 \pm 0.8$	$4.5 \pm 0.9$
$S_2^+/S_4^+$	$159 \pm 13$	$m = -1.6 \pm 0.1$	$S_7^{++} \rightarrow S_4^+ + S_3^+$	$3.8 \pm 0.7$	$3.8 \pm 0.6$
	$69 \pm 10$		$S_3^+ \rightarrow S_2^+ + S$	$2.7 \pm 0.8$	
$S_2^+/S_3^+$	$94 \pm 14$	$m = -1.5 \pm 0.2$	$S_8^{++} \rightarrow S_4^+ + S_4^+$	$1.7 \pm 0.3$	$8.5 \pm 1.8$
	$70 \pm 10$		$S_4^+ \rightarrow S_2^+ + S_2$	$1.8 \pm 0.6$	
	$40 \pm 10$		$S_4^+ \rightarrow S_3^+ + S$	$0.8 \pm 0.4$	
$S^+/S_2^+$	$78 \pm 14$	$m = -1.2 \pm 0.2$	$S_8^{++} \rightarrow S_5^+ + S_3^+$	$2.4 \pm 0.7$	$6.0 \pm 1.4$
	$60 \pm 10$		$S_5^+ \rightarrow S_2^+ + S_3$	$1.1 \pm 0.4$	
	$50 \pm 10$		$S_3^+ \rightarrow S^+ + S_2$	$1.4 \pm 0.6$	
$S^+/S_3^+$	$117 \pm 12.6$	$m = -3.0 \pm 0.3$	$S_6^{++} \rightarrow S_3^+ + S_3^+$	$2.4 \pm 0.5$	$6.0 \pm 1.0$
	$80 \pm 10$		$S_3^+ \rightarrow S^+ + S_2$	$3.6 \pm 1.0$	
$S_2^+/S_2^+$	$67 \pm 14$	$\beta = 1.0 \pm 0.2$	$S_8^{++} \rightarrow S_4^{++} + S_4$	$1.7 \pm 0.5$	$4.2 \pm 0.8$
	$134 \pm 14$	$m = -1.0 \pm 0.1$	$S_4^{++} \rightarrow S_2^+ + S_2^+$	$3.4 \pm 0.8$	
$S^+/S^+$	$56 \pm 14$	$\beta = 1.0 \pm 0.2$	$S_8^{++} \rightarrow S_2^{++} + S_6$	$1.6 \pm 0.9$	$2.3 \pm 0.3$
	$183 \pm 14$	$m = -1.0 \pm 0.1$	$S_2^{++} \rightarrow S^+ + S^+$	$6.3 \pm 1.0$	

**Tab. 4.5:** Peak shape analysis of the ion-ion-coincidence signals recorded after ionization via collisions with  $Xe^{5+}$  ions.  $m$  and  $\beta$  represent the slopes of the long and of the short edge of the correlation plots, respectively



The kinetic energy released in the charge separation step is calculated to be  $6.3 \pm 1.0$  eV, which leads to a charge separation distance before the fission of  $2.3 \pm 0.3$  Å (in neighboring positions). The loss of the neutral  $S_6$  moiety is accompanied by a notably smaller kinetic energy release, namely  $1.6 \pm 0.9$  eV.

Table 4.5 summarizes the analysis of the coincidence correlation plots obtained subsequent to the ionization through collisions with  $Xe^{5+}$  ions accelerated at 10 kV.

It is important to draw attention that for the  $Xe^{5+}$  ion beam case, one can observe that, after ionization, the localization of the charge at opposite site leads to the occurrence of the  $S_3^+$  ion in coincidence with other moieties. The second ionic species recorded depends on whether the parent ion has released or not a neutral prior to charge separation ( $S^+$  and  $S_2^+$ , respectively).

The localization of the charges in the parent ion at second neighboring position (atoms 1 and 3

in Fig. 4.7) has turned out to lead to the appearance of the  $S_2^+/S_4^+$  and  $S^+/S_2^+$  coincidence channels, depending on the size of the initial doubly charged ion immediately before charge separation ( $S_7^{++}$  and  $S_8^{++}$ , respectively).

It has been observed that a charge localization at almost opposite positions (atoms 1 and 4 in Fig. 4.7) is responsible for the occurrence of the  $S_2^+/S_2^+$  and  $S_2^+/S_6^+$  coincidence channels, depending on whether the parent ion has or not released a neutral moiety before charge separation. The symmetric  $S^+/S^+$  coincidence channel only occurs when the two charges are located in the parent ion at neighboring positions prior to fission .

#### 4.1.2.2 $Xe^{10+}$ ion beam

Figure 4.8 presents the correlation plots of the coincidence signals recorded after ionizing sulfur clusters with an ion beam of  $Xe^{10+}$  accelerated at 10 kV. The cation pairs identified were:  $S_2^+/S_4^+$ ,  $S_2^+/S_2^+$  and  $S^+/S^+$ .

The temperature of the second stage of the cluster source (see Chapter 3.2.1 for more details about the experimental setup) was kept constant at  $T = 400$  K during the measurements, thus allowing us to keep the size distribution of the sulfur aggregates constant (mainly  $S_8$ ).

#### $S_2^+/S_4^+$

In this case (see Fig.4.8 (a)), the experimental slope obtained is  $m = -1.4 \pm 0.1$ , which suggests a secondary decay involving the lighter cation. The proposed three body mechanism which describes the process leading to such a slope of the correlation plot is a two step mechanism describing the dissociation of  $S_7^{++}$  as follows:



The kinetic energy released in the charge separation process was determined to be  $2.8 \pm 0.6$  eV, which corresponds to a charge separation distance of  $5.1 \pm 0.9$  Å before the fission (opposite sites in the parent dication). The loss of the  $S$  neutral is accompanied by a smaller kinetic energy release ( $2.8 \pm 0.8$  eV).

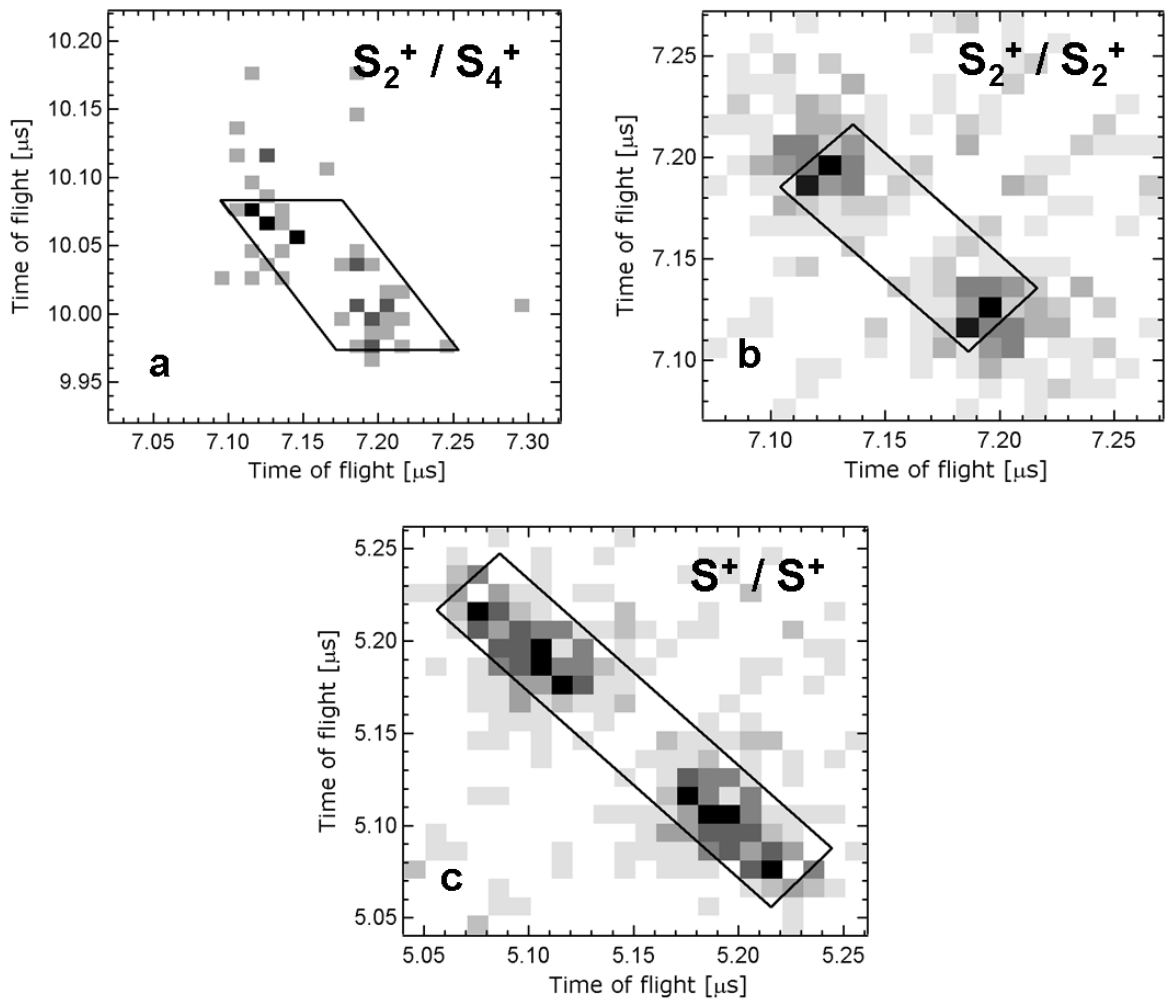
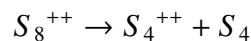


**Fig. 4.8:** Ion-ion-coincidence correlation plots of sulfur aggregates ionized via collisions with  $Xe^{10+}$  ions

### $S_2^+ / S_2^+$

The calculated experimental slope for the  $S_2^+ / S_2^+$  ion pair (see Fig.4.8 (b)) is obtained to be  $m = -1.0 \pm 0.1$ . Considering the composition of the sulfur vapor at the temperature used throughout the experiments, we can consider the doubly charged tetramer  $S_4^{++}$  as originating from  $S_8^{++}$  through the loss of a neutral  $S_4$ . This is consistent with the finding that the secondary slope of the correlation slope is  $\beta = 1.0 \pm 0.1$ . We can, thus, conclude that the mechanism leading to the appearance of this cation pair is described by:





The kinetic energy release for the second step of the dissociation, is  $2.4 \pm 0.6$  eV corresponding to a charge separation distance of  $6.0 \pm 1.3$  Å before the fission (opposite sites in the parent ion). The release of the  $S_4$  neutral moiety is accompanied by a kinetic energy release of  $0.7 \pm 0.4$  eV.

### $S^+/S^+$

For the  $S^+/S^+$  ion pair (see Fig.4.8 (c)), the experimental slope of the correlation plot is calculated to be  $m = -1.0 \pm 0.1$ . This slope suggests a two body dissociation of  $S_2^{++}$ , but considering the composition of the sulfur vapor at our experimental temperature [19](thus, a low concentration of  $S_2$ ) it is assumed that the real ion parent is  $S_8^{++}$ . This is also supported by the fact that the secondary slope of the correlation plot is  $\beta = 1.0 \pm 0.2$ , thus suggesting a deferred charge separation mechanism, as described below:



The kinetic energy released in the charge separation step is calculated to be  $8.5 \pm 1.2$  eV, which leads to a charge separation distance before the fission of  $2.0 \pm 0.3$  Å (neighboring positions in the parent ion). The loss of the  $S_6$  neutral is accompanied by a smaller kinetic energy release ( $1.3 \pm 0.7$  eV).

Table 4.6 summarizes the analysis of the coincidence correlation plots obtained subsequent to the ionization through collisions with  $Xe^{10+}$  ions accelerated at 10 kV.

Ion pair	Edge length (ns)	Edge slope	Proposed mechanism	KER (eV)	CSD (Å)
$S_2^+/S_4^+$	$136 \pm 14$	$m = -1.4 \pm 0.1$	$S_7^{++} \rightarrow S_4^+ + S_3^+$	$2.8 \pm 0.6$	$5.1 \pm 0.9$
	$70 \pm 10$		$S_3^+ \rightarrow S_2^+ + S$	$2.8 \pm 0.8$	
$S_2^+/S_2^+$	$113 \pm 14$	$m = -1.0 \pm 0.1$ $\beta = 1.0 \pm 0.1$	$S_8^{++} \rightarrow S_4^{++} + S_4$	$0.7 \pm 0.4$	$6.0 \pm 1.3$
	$42 \pm 14$		$S_4^{++} \rightarrow S_2^+ + S_2^+$	$2.4 \pm 0.6$	
$S^+/S^+$	$212 \pm 14$	$m = -1.0 \pm 0.1$ $\beta = 1.0 \pm 0.2$	$S_8^{++} \rightarrow S_2^{++} + S_6$	$1.3 \pm 0.7$	$2.0 \pm 0.3$
	$42.3 \pm 14.1$		$S_2^{++} \rightarrow S^+ + S^+$	$8.5 \pm 1.2$	

**Tab. 4.6:** Peak shape analysis of the ion-ion-coincidence signals recorded after ionization via collisions with  $Xe^{10+}$  ions.  $m$  and  $\beta$  represent the slopes of the long and of the short edge of the correlation plots, respectively

It is important to remark that, when ionizing with the  $Xe^{10+}$  ion beam, the localization of the charge in the parent ion prior to charge separation at opposite sites can lead to the occurrence of two different coincidence channels ( $S_2^+/S_4^+$  and  $S_2^+/S_2^+$ ). This depends of whether the doubly charged ion immediately before charge separation is  $S_7^{++}$  or  $S_8^{++}$ , as shown previously in this section.

The localization of the chargesw in the parent ion at neighboring positions leads, as in the case of the  $Xe^{5+}$  ion beam to the occurrence of the  $S^+/S^+$  symmetric coincidence channel.

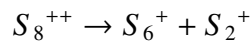
#### 4.1.2.3 $Xe^{15+}$ ion beam

Figures 4.9 show the correlation plots of the coincidence signals recorded after ionizing sulfur clusters with an ion beam of  $Xe^{15+}$  accelerated at 8 kV. The cation pairs identified were:  $S_2^+/S_4^+$ ,  $S_2^+/S_3^+$ ,  $S^+/S^{2+}$ ,  $S_2^+/S_2^+$  and  $S^+/S^+$ .

The temperature of the second stage of the cluster source (see Chapter 3.2.1 for more details about the experimental setup) was kept constant at  $T = 400$  K during the measurements, thus allowing us to keep the size distribution of the sulfur aggregates constant (mainly  $S_8$ ).

#### $S_2^+/S_4^+$

In the case of the  $S_2^+/S_4^+$  cation pair (see Fig.4.9 (a)), the main slope of the correlation plot is determined to be  $m = -0.7 \pm 0.1$ . This slope is interpreted as an indication of a *secondary decay* mechanism [66][60] originating from  $S_8^{++}$ , as described by the process:



The kinetic energy release (*KER*) accompanying the charge separation process is  $2.6 \pm 0.6$  eV which corresponds to a charge separation distance (*CSD*) of  $5.6 \pm 1.1$  Å. This is likely to indicate a charge separation where the charges ar located at opposite sites in the  $S_8$  cluster. The secondary process (the release of the neutral) is accompanied by a kinetic energy release of  $1.4 \pm 0.4$  eV.

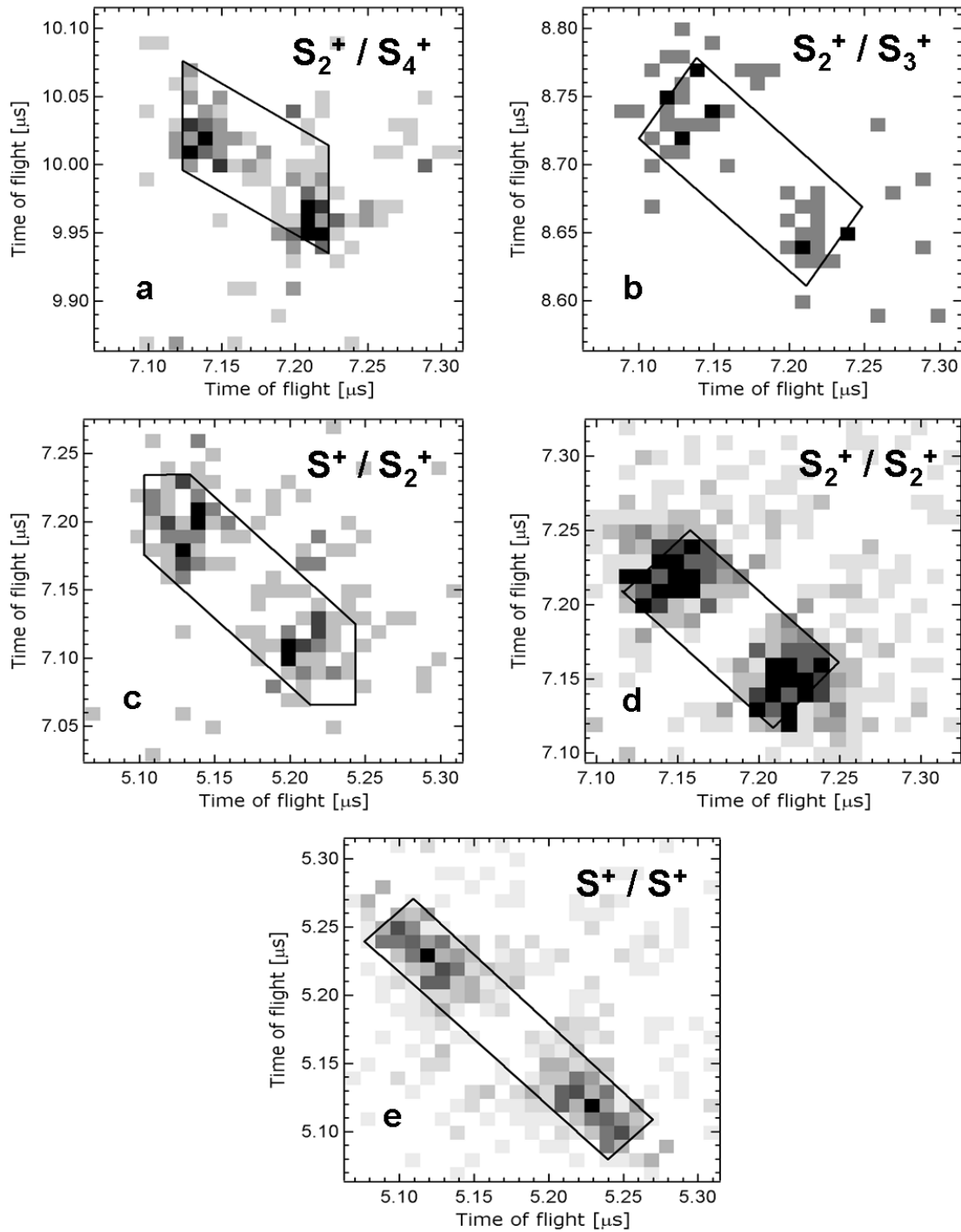


**Fig. 4.9:** Shapes of ion-ion-coincidence signals from sulfur ionic fragments resulting through ionization via collisions with  $Xe^{15+}$  ions

$S_2^+/S_3^+$ 

In the case of the  $S_2^+/S_3^+$  cation pair (see Fig.4.9 (b)), the main slope of the correlation plot is determined to be  $m = -1.0 \pm 0.1$ . This slope is interpreted as an indication of a *deferred charge separation* mechanism [66] originating from  $S_8^{++}$ , as described by the process:

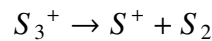


This is consistent with the fact that the slope of the short edges equals  $-1.5 \pm 0.2$ .

The kinetic energy release (*KER*) accompanying the charge separation process is  $3.8 \pm 0.8$  eV which corresponds to a charge separation distance (*CSD*) of  $3.8 \pm 0.7$  Å. This result is likely to indicate a charge separation where the charges are located at second neighboring sites in the  $S_8$  cluster. This conclusion was drawn considering that the  $S-S$  bond length is  $2.055$  Å in the stable  $S_8$  cluster [11, 118, 119, 120]. The first step of the dissociation is accompanied by a kinetic energy release of  $2.07 \pm 0.72$  eV.

 $S^+/S_2^+$ 

For the  $S^+/S_2^+$  ion pair (see Fig.4.9 (c)), the experimental slope of the correlation plot is calculated to be  $m = -1.1 \pm 0.1$ . This slope is interpreted as an indication of a *secondary decay in competition* mechanism [66] originating from  $S_8^{++}$ , as described by the process:



During the charge separation step, an amount of  $4.8 \pm 0.9$  eV energy is released as kinetic energy of the charged fragments. This value corresponds to a charge separation distance of  $3.0 \pm 0.5$  Å prior to the dissociation, equivalent to the charge being localized at second neighboring atomic sites in the parent cluster. The losses of neutral moieties are accompanied by a rather small kinetic energy release, namely  $0.8 \pm 0.3$  eV for the release of the  $S_3$  neutral and  $0.9 \pm 0.5$  eV for the loss of  $S_2$ .

$S_2^+/S_2^+$ 

For the  $S_2^+/S_2^+$  ion pair (see Fig.4.9 (d)), the experimental slope of the correlation plot is calculated to be  $m = -1.0 \pm 0.1$ . Considering the composition of the sulfur vapor at the temperature used throughout the experiments, we can consider the doubly charged tetramer  $S_4^{++}$  as originating from  $S_8^{++}$  through the loss of a neutral  $S_4$ . This is consistent with the finding that the secondary slope of the correlation slope is  $\beta = 1.0 \pm 0.2$ . We can, thus, conclude that the mechanism leading to the appearance of this cation pair is described by:



During the charge separation step, an amount of  $3.0 \pm 0.7$  eV energy is released as kinetic energy of the charged fragments. This value corresponds to a charge separation distance of  $4.7 \pm 0.9$  Å prior to the dissociation. The first step of the dissociation (the loss of the  $S_4$  moiety) is accompanied by a kinetic energy release of  $1.2 \pm 0.5$  eV.

 $S^+/S^+$ 

For the  $S^+/S^+$  ion pair (see Fig.4.9 (e)), the correlation plot consists of a parallelogram with the slope of the longest edge of  $m = -1.0 \pm 0.1$ . Considering that  $S_8$  is the major component in the gas phase at the experimental evaporation conditions ( $T = 400K$ )[19] it is considered unlikely that this ion pair occurs from the two-body dissociation of  $S_2^{++}$ , but instead, from the dissociation of  $S_8^{++}$ , thus a deferred charge separation. This conclusion was drawn considering also that the secondary slope of the parallelogram is  $\beta = 1.0 \pm 0.1$ . Therefore, the proposed mechanism would be:



The kinetic energy released in the charge separation step is  $8.5 \pm 1.2$  eV which corresponds to a charge separation distance of  $2.0 \pm 0.3$  Å prior to the dissociation. The loss of the  $S_6$  aggregate in the first stage of the fission is accompanied by a kinetic energy release of  $1.3 \pm 0.7$  eV.

Table 4.7 summarizes the analysis of the coincidence correlation plots obtained subsequent to the ionization through collisions with  $Xe^{15+}$  ions accelerated at  $8kV$ .

Based on the analysis presented earlier in this section, we can conclude that, similar to the lower charge cases, the  $S^+/S^+$  symmetric coincidence channel only occurs when the two charges are

Ion pair	Edge length (ns)	Edge slope	Proposed mechanism	KER (eV)	CSD (Å)
$S_2^+/S_4^+$	$122 \pm 14$	$m = -0.7 \pm 0.1$	$S_8^{++} \rightarrow S_6^+ + S_2^+$	$2.6 \pm 0.6$	$5.6 \pm 1.1$
	$70 \pm 10$		$S_6^+ \rightarrow S_4^+ + S_2$	$1.4 \pm 0.4$	
$S_2^+/S_3^+$	$155 \pm 14$	$m = -1.0 \pm 0.1$ $\beta = 1.5 \pm 0.2$	$S_8^{++} \rightarrow S_5^{++} + S_3$	$2.1 \pm 0.7$	$3.8 \pm 0.6$
	$72 \pm 14$		$S_5^{++} \rightarrow S_2^+ + S_3^+$	$3.8 \pm 0.8$	
$S^+/S_2^+$	$155 \pm 14$	$m = -1.1 \pm 0.1$	$S_8^{++} \rightarrow S_5^+ + S_3^+$	$4.8 \pm 0.9$	$3.0 \pm 0.5$
	$50 \pm 10$		$S_5^+ \rightarrow S_2^+ + S_3$	$0.8 \pm 0.3$	
	$40 \pm 10$		$S_3^+ \rightarrow S^+ + S_2$	$0.9 \pm 0.5$	
$S_2^+/S_2^+$	$127 \pm 14$	$m = -1.0 \pm 0.1$ $\beta = 1.0 \pm 0.1$	$S_8^{++} \rightarrow S_4^{++} + S_4$	$1.2 \pm 0.5$	$4.73 \pm 0.9$
	$56 \pm 14$		$S_4^{++} \rightarrow S_2^+ + S_2^+$	$3.0 \pm 0.7$	
$S^+/S^+$	$212 \pm 14$	$m = -1.0 \pm 0.1$ $\beta = 1.0 \pm 0.1$	$S_8^{++} \rightarrow S_2^{++} + S_6$	$1.3 \pm 0.7$	$2.0 \pm 0.3$
	$42 \pm 14$		$S_2^{++} \rightarrow S^+ + S^+$	$8.5 \pm 1.2$	

**Tab. 4.7:** Peak shape analysis of the ion-ion-coincidence signals recorded after ionization via collisions with  $Xe^{15+}$  ions.  $m$  and  $\beta$  represent the slopes of the long and of the short edge of the correlation plots, respectively

localized at neighboring positions (atoms 1 and 2 in Fig. 4.7) in the doubly charged parent ion. A localization of the two charges at second neighboring positions will lead to the occurrence of the  $S_2^+/S_3^+$  and  $S^+/S_2^+$  cation pairs.

It has been observed that the localization of charges at opposite position in the parent ion is responsible for the occurrence of the  $S_2^+/S_4^+$  and  $S_2^+/S_2^+$  coincidence channels. As it has been shown earlier in this section, the appearance of the two cation pairs is dependent on whether the first fragmentation process is a charge separation fission ( $S_2^+/S_4^+$ ) or a release of a neutral moiety ( $S_2^+/S_2^+$ ).

#### 4.1.2.4 $Xe^{20+}$ ion beam

Figure 4.10 shows the correlation plots of the coincidence signals recorded after ionizing sulfur clusters with an ion beam of  $Xe^{20+}$  accelerated at 10 kV. The cation pairs identified were:  $S_2^+/S_6^+$ ,  $S_2^+/S_4^+$ ,  $S_2^+/S_3^+$ ,  $S^+/S^{2+}$ ,  $S_2^+/S_2^+$ ,  $S^+/S^+$ , as seen in Fig. 4.2.

The temperature of the second stage of the cluster source (see Chapter 3.2.1 for more details about the experimental setup) was kept constant at  $T = 400$  K during the measurements, thus allowing us to keep the size distribution of the sulfur aggregates constant (mainly  $S_8$ ).

$\mathbf{S}_2^+/\mathbf{S}_6^+$ 

In the case of the  $S_2/S_6$  cation pair (see Fig.4.10 (a)), the experimental slope of the correlation plot is determined to be  $m = -1.0 \pm 0.1$ . This slope is interpreted as an indication of a *two-body dissociation* mechanism [66] originating from  $S_8^{++}$ , as described by the process:



The kinetic energy release (*KER*) accompanying this fragmentation process is  $3.2 \pm 0.8$  eV which corresponds to a charge separation distance (*CSD*) of  $4.5 \pm 0.9$  Å. This result is likely to indicate a charge separation where the charges are located at almost opposite sites in the  $S_8$  cluster, considering our experimental uncertainty as well as the  $S - S$  bond length which is  $2.055$  Å in the stable  $S_8 D_{3h}$  isomer. [11, 118, 119, 120].

 $\mathbf{S}_2^+/\mathbf{S}_4^+$ 

The signal  $S_2^+/S_4^+$  is long-shaped (see Fig.4.10 (b)) with a main slope  $m = -0.9 \pm 0.1$ . An experimental slope smaller than  $-1$  indicates a *secondary decay* process involving the heavier cation[60]. The full parallelogram in Fig.4.10 (b) corresponds to the fission of  $S_7^{++}$ , as described below.



Still, the secondary decay scenario does not completely describe the fragmentation process, as it would lead to a maximum slope of  $-0.8$ . It can be deduced that the  $S_2^+/S_4^+$  cation pair occurs also from the *two-body dissociation* of  $S_6^{++}$  (see 4.18), process whose correspondent is represented in (see Fig.4.10 (b)) by the dashed line of slope  $m = -1$ .



Therefore it was concluded that the  $S_2^+/S_4^+$  ion pair appears as a result of a superposition of the two distinct paths described in 4.17 and 4.18. Based on the mass distribution of neutrals in the cluster beam, it is considered that both  $S_7^{++}$  and  $S_6^{++}$  are most likely formed from  $S_8^{++}$  [19]. The kinetic energy release which accompanies the two paths are  $5.2 \pm 0.9$  eV for 4.17 and  $3.6 \pm 1.4$  eV for 4.18, which correspond to charge separation distances of  $2.8 \pm 0.4$  Å and  $4.0 \pm 1.1$  Å, respectively. These charge separation distances indicate that the two charges are located at

second neighboring and adjacent sites, respectively. The first step of the mechanism described by 4.17 is accompanied by a kinetic energy release of  $2.5 \pm 0.6$  eV.

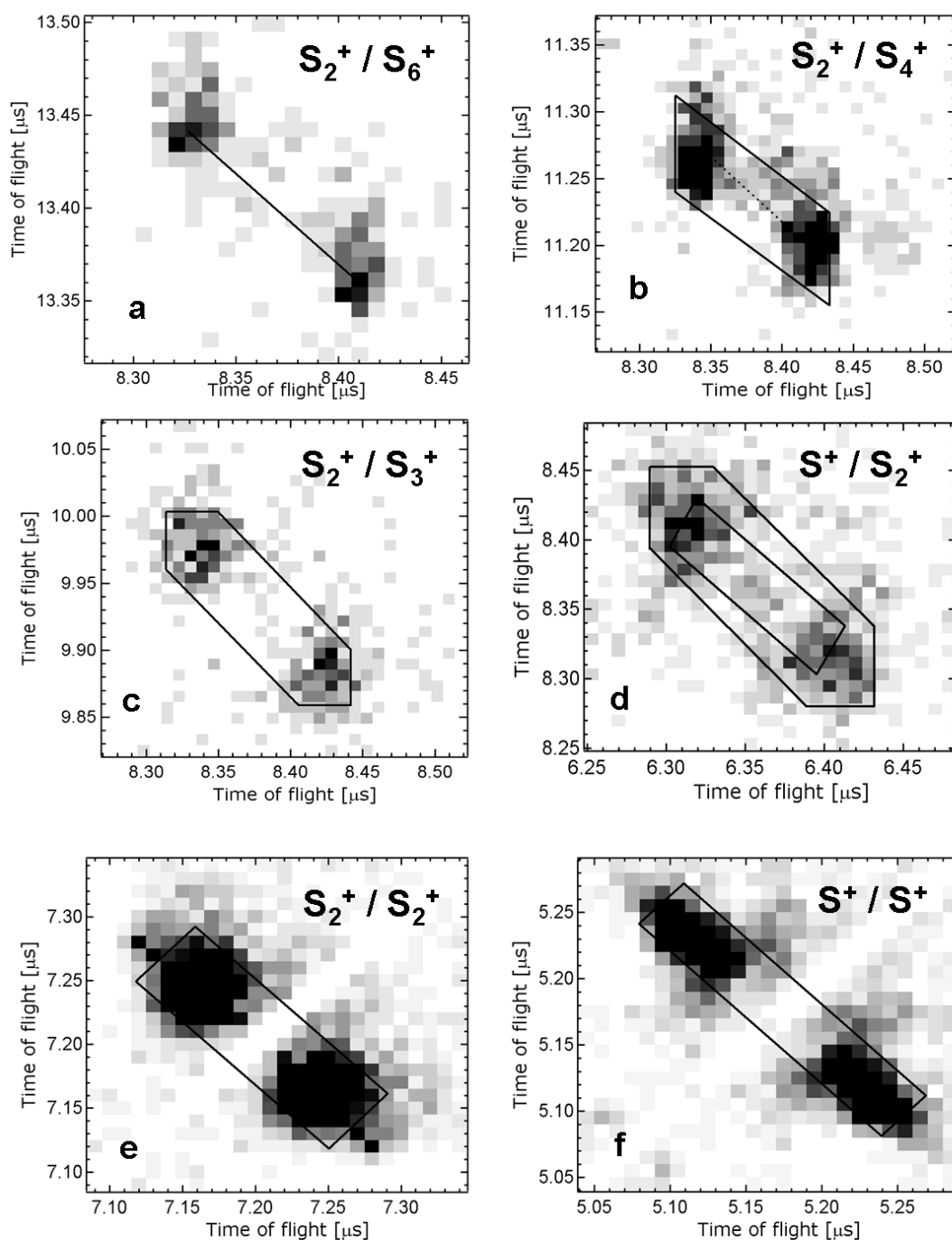


**Fig. 4.10:** Ion-ion-coincidence correlation plots of sulfur aggregates ionized via collisions with  $Xe^{20+}$  ions

$S_2^+/S_3^+$ 

The experimental slope obtained for the  $S_2^+/S_3^+$  correlation plot (see Fig.4.10 (c)) is determined to be  $m = -1.2 \pm 0.1$ . An experimental slope different from  $-1$  indicates a fragmentation process involving at least three fragments, meaning that at least one of the charged particles is releasing a neutral subsequent to the charge separation [60][66]. A slope bigger than  $-1$  indicates a secondary loss of a neutral from the lighter cation. Still, there is no three-body process that can explain the fragmentation process and lead to such an experimental slope, as the minimum slope for such a secondary decay would be  $-1.5$ . Losses of heavier neutrals are expected to lead to even higher slopes. Thus, it can be concluded that the the process leading to the appearance of this cation pair involves releases of neutrals from both cations subsequent to charge separation, namely a *secondary decay in competition* mechanism as described by 4.19. The parallelogram in Fig.4.10 (c) corresponds to the fission of  $S_7^{++}$  so that  $S_4^+$  and  $S_3^+$  are formed.



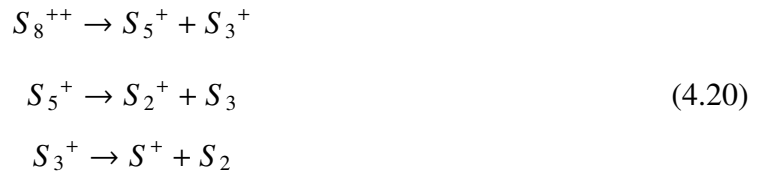
The kinetic energy release from the charge separation process is calculated to be  $4.2 \pm 0.7$  eV, which requires a charge separation distance in the  $S_7^{++}$  cluster of  $3.4 \pm 0.5$  Å. Due to the very low concentration of  $S_7$  in the neutral cluster beam[19] the start of this process from  $S_7^{++}$  was discounted, the doubly charged cation being most likely a fragment of  $S_8^{++}$ .

The loss of neutral moieties are accompanied rather small kinetic energy releases, namely  $0.80 \pm 0.4$  eV for the release of the  $S$  neutral from the decay of  $S_4^+$  and  $0.6 \pm 0.3$  eV for the loss of  $S$  from the  $S_3^+$  aggregate.

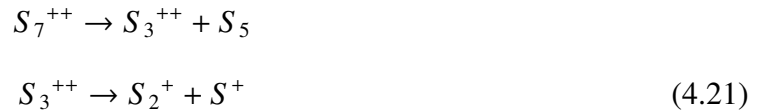
 $S^+/S_2^+$ 

The calculated slope of the  $S^+/S_2^+$  signal is  $m = -1.1 \pm 0.1$  (see Fig.4.10 (d)). This interpreted as an evidence for two competing processes. The first one is a secondary decay in competition involving the intermediate formation of  $S_7^{++}$ , which would lead to a plot with a slope of  $m = -1.125$ , depicted in Fig.4.10 (d) by the hexagon. The second process is a deferred charge separation process starting from  $S_8^{++}$  which would result in a correlation plot with a main slope of  $m = -1$  and a secondary slope equal to 2, which is represented in Fig.4.10 (d) by the rectangle. The proposed mechanisms for the fragmentation leading to the occurrence of this experimental slope are described by the following two processes:

process 1:



process 2:



The kinetic energy released in the charge separation steps of the two processes is determined to be  $4.8 \pm 0.7$  eV (process 1) and  $9.6 \pm 2.2$  eV (process 2), corresponding to charge separation distances of  $3.0 \pm 0.4$  Å and  $1.5 \pm 0.3$  Å, respectively. The last two steps of *process 1* are accompanied by small kinetic energy releases of  $1.1 \pm 0.3$  and  $1.0 \pm 0.4$  eV, respectively, while in the first stage of *process 2* a kinetic energy release of  $0.5 \pm 0.3$  eV has been determined.

### $S_2^+/S_2^+$

The calculated experimental slope for the  $S_2^+/S_2^+$  ion pair (see Fig.4.10 (e)) is obtained to be  $m = -1.0 \pm 0.1$ . Considering the composition of the sulfur vapor at the temperature used throughout the experiments, we can consider the doubly charged tetramer  $S_4^{++}$  as originating from  $S_8^{++}$  through the loss of a neutral  $S_4$ . This is consistent with the finding that the secondary slope of the correlation slope is  $\beta = 1.0 \pm 0.2$ . We can, thus, conclude that the mechanism leading to the appearance of this cation pair is described by:



The kinetic energy released in the charge separation process is  $6.3 \pm 1.0$  eV, which corresponds to a charge separation distance of  $2.3 \pm 0.3$  Å prior to the dissociation. The loss of the  $S_4$  aggregate in the first stage of the fission is accompanied by a kinetic energy release of  $1.2 \pm 0.3$  eV.

### $S^+/S^+$

For the  $S^+/S^+$  ion pair (see Fig.4.10 (f)), the correlation plot consists of a parallelogram with the slope of the longest edge of  $m = -1.0 \pm 0.1$ . Considering that  $S_8$  is the major component in the

gas phase at the experimental evaporation conditions ( $T = 400K$ )[19] it is considered unlikely that this ion pair occurs from the two-body dissociation of  $S_2^{++}$ , but instead, from the dissociation of  $S_8^{++}$ , thus a deferred charge separation. This conclusion was drawn considering also that the secondary slope of the parallelogram is  $\beta = 1.0 \pm 0.2$ . Therefore, the proposed mechanism would be:



The kinetic energy released in the charge separation process is  $8.5 \pm 1.2 eV$ , which corresponds to a charge separation distance of  $1.7 \pm 0.2 \text{ \AA}$  prior to the dissociation. The loss of the  $S_6$  aggregate in the first stage of the fission is accompanied by a kinetic energy release of  $0.9 \pm 0.7 eV$ .

Table 4.8 summarizes the analysis of the coincidence correlation plots obtained subsequent to the ionization through collisions with  $Xe^{20+}$  ions accelerated at  $10kV$ .

Ion pair	Edge length (ns)	Edge slope	Proposed mechanism	KER (eV)	CSD ( $\text{\AA}$ )
$S_2^+/S_6^+$	$113 \pm 14$	$m = -1.0 \pm 0.1$	$S_8^{++} \rightarrow S_2^+ + S_6^+$	$3.2 \pm 0.8$	$4.5 \pm 0.9$
$S_2^+/S_4^+$	$144 \pm 11$	$m = -0.8$	$S_7^{++} \rightarrow S_5^+ + S_2^+$	$5.2 \pm 0.9$	$2.8 \pm 0.4$
	$73 \pm 8$		$S_5^+ \rightarrow S_4^+ + S$	$2.5 \pm 0.6$	
	$80 \pm 14$	$m = -1$	$S_6^{++} \rightarrow S_4^+ + S_2^+$	$3.6 \pm 1.4$	$4.0 \pm 1.1$
$S_2^+/S_3^+$	$138 \pm 11$	$m = -1.2 \pm 0.1$	$S_7^{++} \rightarrow S_4^+ + S_3^+$	$4.2 \pm 0.7$	$3.4 \pm 0.5$
	$40 \pm 8$		$S_4^+ \rightarrow S_3^+ + S$	$0.8 \pm 0.4$	
	$32 \pm 8$		$S_3^+ \rightarrow S_2^+ + S$	$0.6 \pm 0.3$	
$S^+/S_2^+$	$154 \pm 11$	$m = -1.125$	$S_8^{++} \rightarrow S_5^+ + S_3^+$	$4.8 \pm 0.7$	$3.0 \pm 0.4$
	$59 \pm 8$		$S_5^+ \rightarrow S_2^+ + S_3$	$1.1 \pm 0.3$	
	$42 \pm 8$		$S_3^+ \rightarrow S^+ + S_2$	$1.0 \pm 0.4$	
	$37 \pm 11$	$\beta = 2$	$S_7^{++} \rightarrow S_3^{++} + S_5$	$0.5 \pm 0.3$	$1.5 \pm 0.3$
	$130 \pm 14$	$m = -1$	$S_3^{++} \rightarrow S_2^+ + S^+$	$9.6 \pm 2.2$	
$S_2^+/S_2^+$	$56 \pm 14$	$\beta = 1.0 \pm 0.2$	$S_8^{++} \rightarrow S_4^{++} + S_4$	$1.2 \pm 0.3$	$4.2 \pm 0.8$
	$134 \pm 14$	$m = -1 \pm 0.1$	$S_4^{++} \rightarrow S_2^+ + S_2^+$	$3.4 \pm 0.8$	
$S^+/S^+$	$42 \pm 14$	$\beta = 1.0 \pm 0.2$	$S_8^{++} \rightarrow S_2^{++} + S_6$	$0.9 \pm 0.7$	$1.7 \pm 0.2$
	$212 \pm 14$	$m = -1.0 \pm 0.1$	$S_2^{++} \rightarrow S^+ + S^+$	$8.5 \pm 1.2$	

**Tab. 4.8:** Peak shape analysis of the ion-ion-coincidence signals recorded after ionization via collisions with  $Xe^{20+}$  ions.  $m$  and  $\beta$  represent the slopes of the long and of the short edge of the correlation plots, respectively

Based on the analysis presented in this section, we can conclude that the localization of the charges in the doubly charged parent ion at neighboring positions (atoms 1 and 2 in Fig. 4.7) will result in the occurrence of symmetric coincidence channels ( $S_2^+/S_2^+$  and  $S^+/S^+$ ).

When the two charges are located at second neighboring sites before fission, the observed cation pairs are  $S_2^+/S_3^+$  and  $S^+/S_2^+$ , irrespective of the parent ion.

Similarly to the ionization using the  $Xe^{5+}$  ion beam, when ionizing through collisions with  $Xe^{20+}$  ions we note that a localization of the charges at almost opposite atoms in the  $S_8^{++}$  parent ion (positions 1 and 4 in Fig. 4.7) will lead to the occurrence of the  $S_2^+/S_6^+$  ion pair. If the doubly charged initial ion is releasing neutral moieties prior to charge separation, the fragmentation process will lead to the appearance of the  $S_2^+/S_4^+$  coincidence channel.

It has also been observed that when the charges in the parent ion are localized at opposite sites (atoms 1 and 5 in Fig. 4.7) the doubly charged ion will fragment via a two-body dissociation mechanism leading to the  $S_2^+/S_4^+$  ion pair.

### 4.1.3 Concluding Remarks

Sulfur clusters have been investigated as a function of temperature, at constant ionization energy, as well as at constant temperature by making use of highly charged ion beams with various energies.

It has been shown that, in agreement to earlier published results [19], on increasing the temperature of the sulfur vapor, the amount of heavier sulfur aggregates ( $S_8$  and  $S_7$ ) decreases. At the same time, the intensity of the smaller sulfur moieties ( $S_2$  and  $S$ ) increases.

Experiments on the fragmentation of sulfur clusters after ionization with highly charged ion beams have been performed for the first time. The analysis of the various fission processes has shown that the symmetric charge separation channels ( $S^+/S^+$ ,  $S_2^+/S_2^+$ ) are constantly more intense than the asymmetric ones ( $S_2^+/S_6^+$ ,  $S_2^+/S_4^+$ ,  $S_2^+/S_3^+$ ,  $S^+/S_2^+$ ,  $S^+/S_3^+$ ).

It is important to note that, irrespective of the charge of the ion beam use for ionization, a charge localization at neighboring atoms in the parent cluster ( $S_8^{++}$ ) will lead to the appearance of the ( $S^+/S^+$  symmetric ion-ion coincidence channel. An exception is the occurrence of the  $S_2^+/S_2^+$  cation pair after ionization with the  $Xe^{20+}$  ion beam.

Another important point to mention is that no two body dissociation path is observed for ion beams with intermediate charge ( $Xe^{10+}$  and  $Xe^{15+}$ ). Such processes are recorded only for the  $Xe^{5+}$  and  $Xe^{20+}$  ion beams, and are originating from  $S_8^{++}$ .

We have observed that charge localization at second neighboring positions (e. g. positions 1 and 3 in Fig. 4.7) will mostly lead to the occurrence of the  $S^+/S_2^+$  or  $S_2^+/S_3^+$  cation pairs, depending on the ionizing ion beam. An exception is the occurrence of the  $S_2^+/S_4^+$  coincidence channel, occurring after the ionization with the  $Xe^{5+}$  ion beam.

The localization of the charges in the parent ion at opposite positions (atoms 1 and 5 in Fig. 4.7) leads to the occurrence of the  $S_2^+/S_4^+$  and  $S_2^+/S_2^+$  ion pairs, depending on the charge of the ionizing ion beam. For the ionization using the  $Xe^{5+}$  ion beam, however, such a localization of the charges in the parent ion leads to the occurrence of the  $S_2^+/S_3^+$  and  $S^+/S_3^+$  coincidence channels.

## 4.2 COLTRIMS Investigations of Sulfur Clusters

The COLTRIMS setup described in Chapter 3.3.2. was employed for investigating the fragmentation of sulfur clusters after inner-shell excitation. Synchrotron radiation from the U49/2-PGM1 at BESSY (see Chapter 3.2.3. for more details) has been used in the single bunch mode. Experiments have been performed below and above the sulfur 2p-edge ( $h\nu = 158$  eV and  $h\nu = 174$  eV, respectively) as well as above the sulfur 2s resonance ( $h\nu = 235$  eV) [114, 121]. The experiments were performed at the temperature of  $400 \pm 3$  K.

As the residual gas contains  $N_2$  whose kinetic energy release spectrum has been previously investigated [122, 123], calibration measurements were performed at  $h\nu = 419$  eV, similar to the measurements of Weber *et. al.*[124] and Rolles *et. al.*[125]. This photon energy lies just above the nitrogen 1s edge, such that the emitted electrons and ions are expected to have a kinetic energy of about 9 eV.

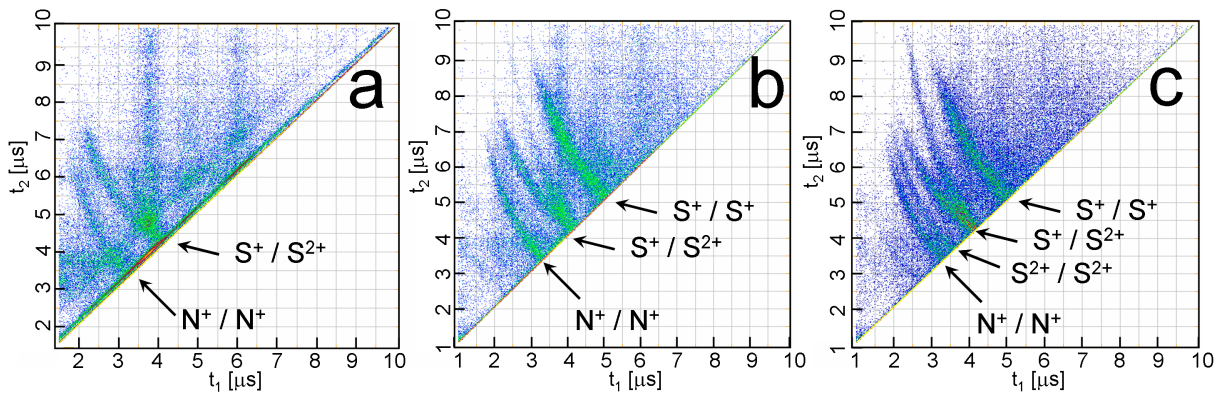


**Fig. 4.11:** Photoion-photoion-coincidence spectra of sulfur clusters recorded at  $T = 400$  K (see text for details)

Figure 4.11 shows ion-ion-coincidence spectra of sulfur clusters as recorded after excitation with photon energies of 158.8 eV (a), 174 eV (b) and 235 eV (c).

For the performed experiments, as already mentioned in Chapter 3.3.2, the electric field used for the extraction and acceleration of the ions towards the detector was  $E = 6$  V/cm. The magnetic field used to confine the electrons within the detectable area was produced by a pair of Helmholtz coils, and the field was set to a value of 10 Gauss.

Figure 4.12 (a) presents in color-code the calculated radius of the ion detector (in mm) plotted versus the flight time of the ions (in ns) [126]. Figure 4.12 (b) depicts in color code the calculated maximum energy resolution of the ion detector. Both theoretical calculations have been made under the assumption that the kinetic energy of the ions with  $m/q = 32$  is within the (0-7) eV interval.

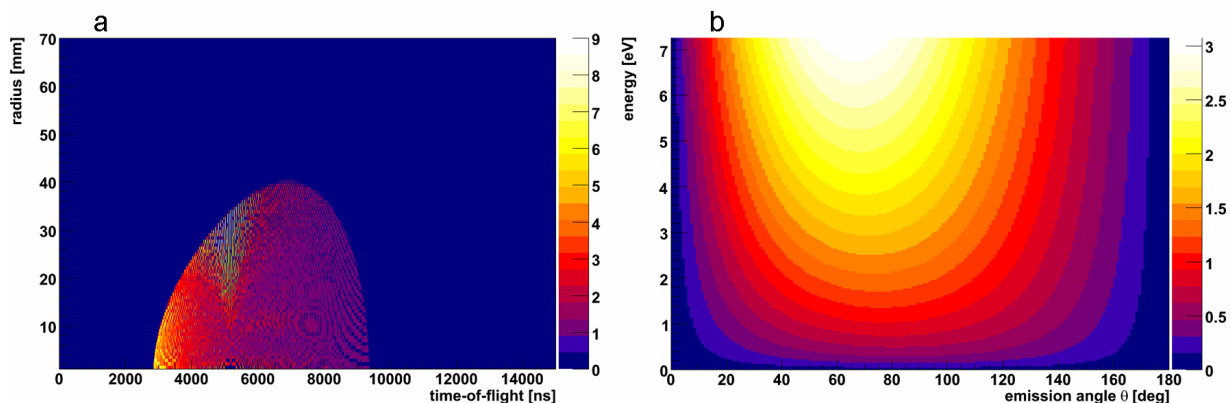


**Fig. 4.12:** Radius of the detector vs. the time-of-flight of the ion (a) and the calculated energy resolution of the ion detector (b) [126] (see text for details)

Possible errors may occur from the fact that it has been considered that the interaction region is a volume of  $5 \times 5 \times 2 \text{ mm}^3$ , that the delay line anode has a space resolution of 0.5 mm and that the time resolution for the time of flight is of the order of 1 ns.

For the coincidence measurements the recorded electrons were used as start signal. However, the electrons have also a definite flight time, so that in order to extract the initial moment of the reaction ( $t_0$ ) one needs to also record the bunch marker signal from the synchrotron beam line. As the revolution period of the electron bunch in the synchrotron storage ring is 800 ns (see Chapter 3.2.3. for details), one can set the condition that  $t_0$  is marked by the first bunch marker that comes before the electron, with the condition that the flight time of the electron is shorter than 800 ns.

### 4.2.1 Identification of the Fragmentation Channels and Calibration

A great deal of effort has been invested in the last years in the investigation of the  $N_2$  molecule with the help of position sensitive coincidence techniques [124, 127, 128, 129, 130] around the N-1s absorption edge.

As there is such a vast literature available for comparison, it was considered that measurements on  $N_2$  from the residual gas at the  $\sigma^*$  resonance (419 eV) can serve as a good calibration of the spectrometer.

Figure 4.13 (b) presents the recorded PEPICO spectrum as recorded after ionization at the photon energy  $h\nu = 419 \text{ eV}$ . The spectrum was recorded at the temperature  $T = 400 \pm 3 \text{ K}$ . As expected, the most intense coincidence channel is  $N^+/N^+$  corresponding to the break up of the  $N_2$  molecule. Other rather weak channels observed are  $N^{2+}/N^{2+}$  and  $S^+/S^{2+}$ .

In Fig. 4.13 (a) a simulated coincidence spectrum [131] as obtained from applying Eq. 3.17 is presented. The simulated spectrum helps one to easier identify the coincidence channels.

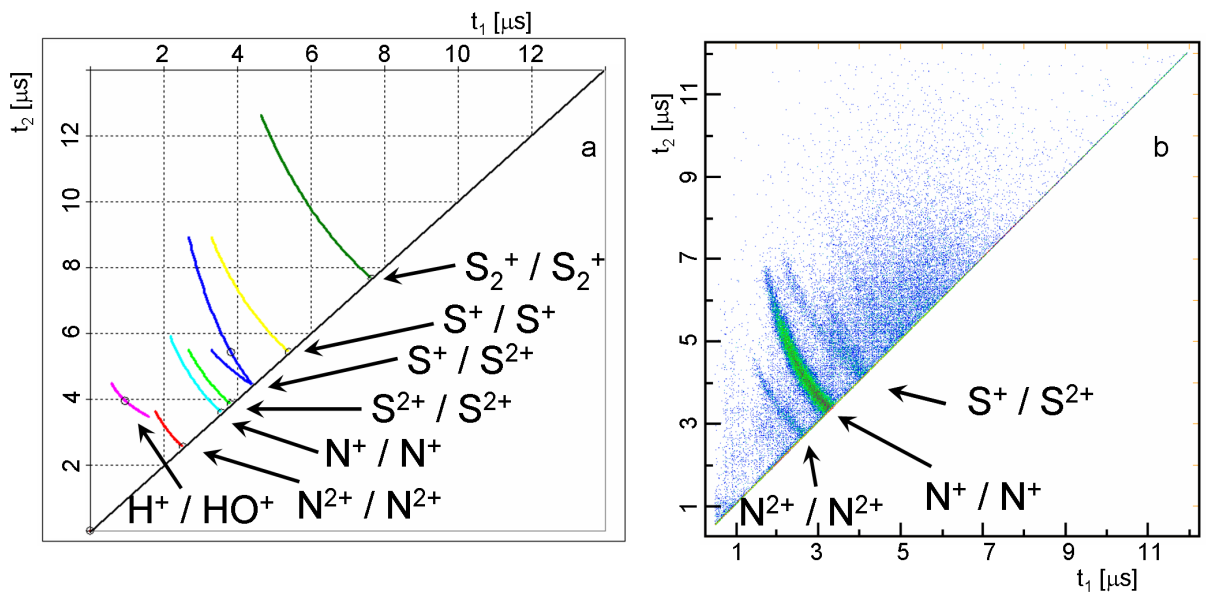


**Fig. 4.13:** Ion-ion coincidence spectrum after ionization with  $h\nu = 419$  eV (see text for details)

By plotting the relative momenta of the ions on one axis versus the relative momenta of the ions on the other two axes, one obtains a sphere in the momentum space. A projection of the momentum sphere on the (xy) plane is presented in Fig. 4.14 (a).

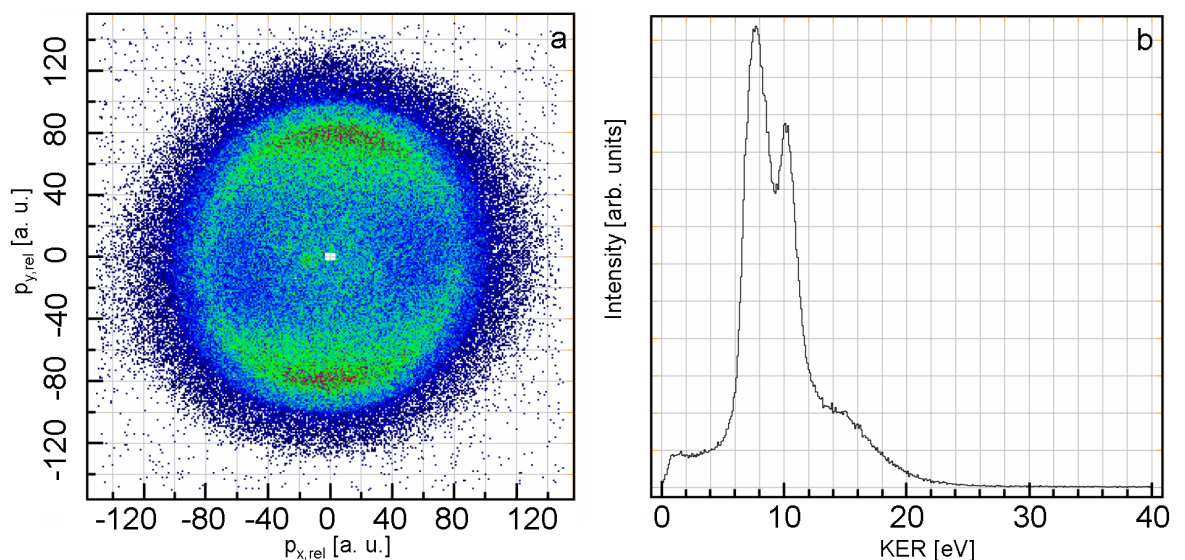


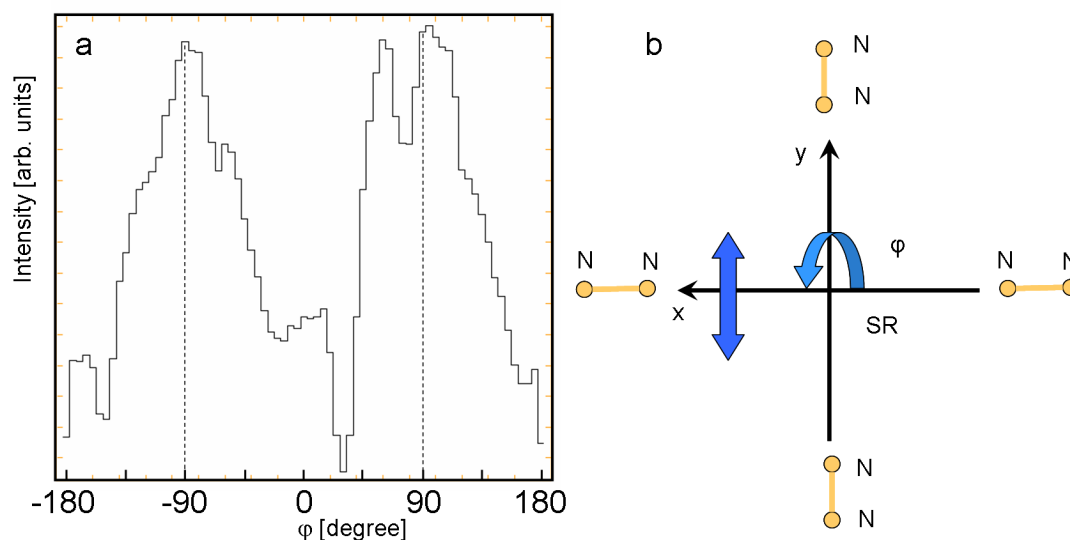
**Fig. 4.14:** Momentum distribution and KER for the  $\text{N}^+ / \text{N}^+$  channel after ionization with  $h\nu = 419$  eV (see text for details)

Knowing the relative momenta of the ions, one can proceed further in calculating the kinetic energy of the fragments emerging from the Coulomb explosion. The straightforward method to calculate the KER of the particles is to make use of Eq. 3.14. The obtained KER for the  $N^+/N^+$  fragmentation channel is depicted in Fig. 4.14 (b).

This result is in good agreement with the earlier reported measurements of Weber *et. al.* [124], with the reserve that the present experiment did not make use of a supersonic molecular gas jet but of the  $N_2$  from the residual gas. This means that the interaction region is not confined to a small volume such as in the experiment of Weber *et. al.*, and thus the resolution is worse.

Figure 4.15 (a) presents the kinetic energy distribution of the  $N^+/N^+$  coincidence channel as a function of the angle between the emission direction and the direction of the synchrotron radiation,  $\varphi$ . The kinetic energy release distribution is calculated as the sum of all fragment kinetic energies for all  $\varphi$  angles.

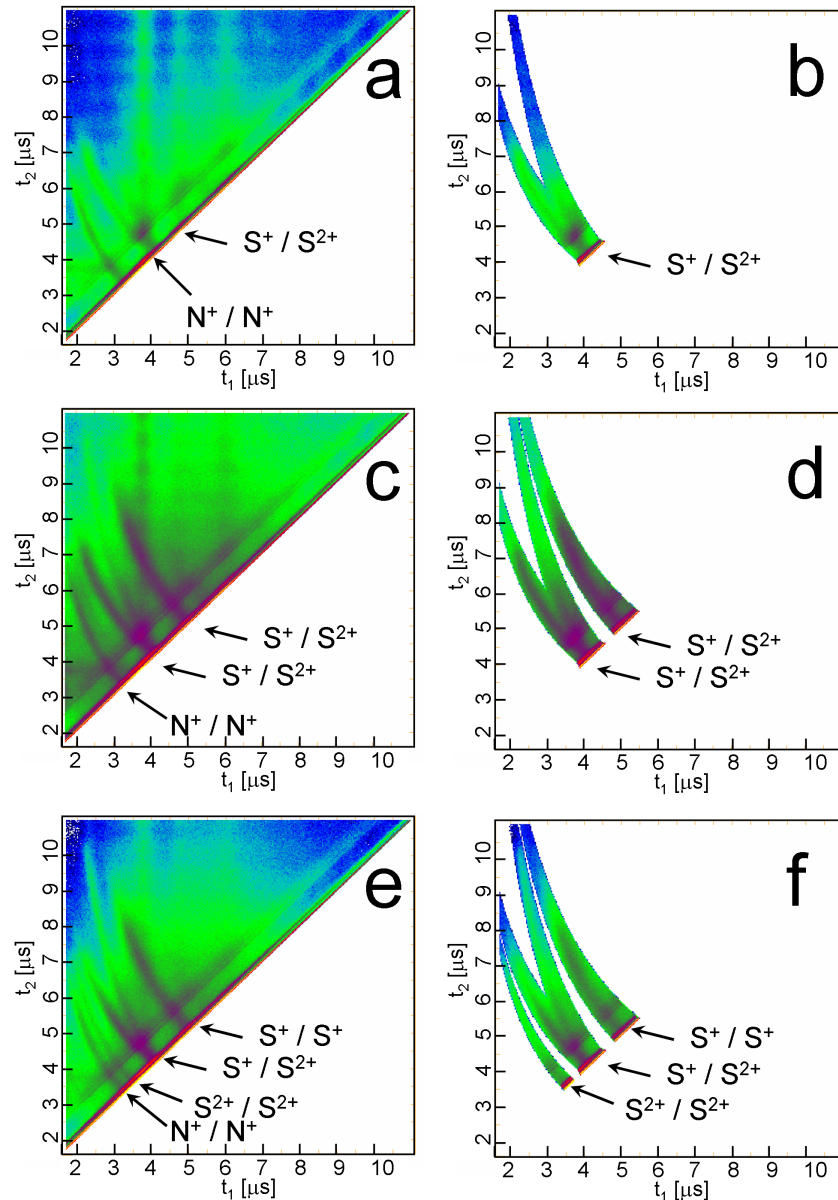
For the U49/2-PGM1 beam line it is known that the electrical component of the electromagnetic wave is perpendicular to the direction of propagation of the beam and perpendicular to the axis of the spectrometer. One can notice that there is a strong angular dependence of the KER on the angle  $\varphi$ , with prominent maxima at  $\pm 90^\circ$  and with minima located at  $0^\circ$  and  $\pm 180^\circ$ . This means that the ionization and the fragmentation processes are favored for the molecules oriented parallel to the polarization direction, as depicted in Fig. 4.15 (b), while for the perpendicular orientation these processes are inhibited.



**Fig. 4.15:** KER distribution of the  $N^+/N^+$  channel after ionization with  $h\nu = 419$  eV as a function of the  $\varphi$  angle (see text for details)

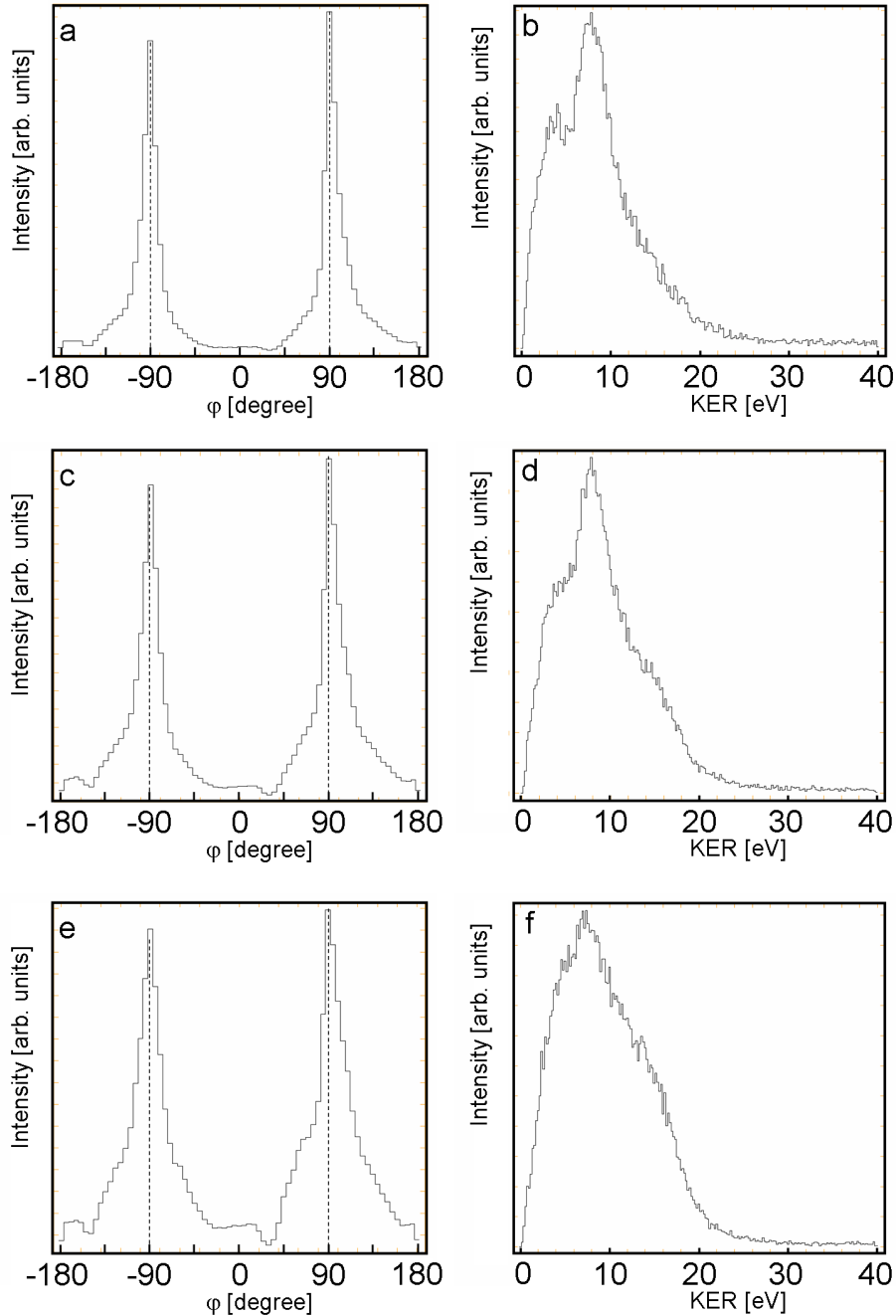
### 4.2.2 Investigation of sulfur clusters as a function of the ionization energy

Figure 4.16 presents the original photoion-photoion-coincidence spectra as recorded after ionization with  $h\nu = 158$  eV (a),  $h\nu = 174$  eV (c) and  $h\nu = 235$  eV (e). On the right side of Fig. 4.16 the same spectra are presented after extracting the sulfur coincidence channels based on the simulated spectrum from Fig. 4.13.



**Fig. 4.16:** Photoion-photoion-coincidence spectra of sulfur clusters as recorded after ionization with  $h\nu = 158$  eV ((a) and (b)),  $h\nu = 174$  eV ((c) and (d)) and  $h\nu = 235$  eV ((e) and (f)).

The kinetic energy release distributions for the  $S^+/S^{2+}$  coincidence channel as recorded after ionization with  $h\nu = 158$  eV,  $h\nu = 174$  eV and  $h\nu = 235$  eV are presented in Fig. 4.17 (a), (c) and (e), respectively, as a function of the  $\varphi$  angle .



**Fig. 4.17:** KER distribution and KER distribution as a function of the  $\varphi$  angle for the  $S^+/S^{2+}$  channel after ionization with  $h\nu = 158$  eV ((a) and (b)),  $h\nu = 174$  eV ((c) and (d)) and  $h\nu = 235$  eV ((e) and (f)) (see text for details)

One notices that, similar to the break-up of the  $N_2^{2+}$  molecule presented in the previous section, the graphs in Fig. 4.17 (a), (c) and (e) present maxima at  $\pm 90^\circ$  and minima at  $0^\circ$  and  $\pm 180^\circ$ .

Taking into account that the broadening of the coincidence signal can be partly caused by losses of neutrals, the maxima and minima in Fig. 4.17 (a), (c) and (e) can be interpreted as an indication of the fact that the sulfur aggregates which are favored to dissociate are the ones in which the axis passing through the centers of the two ions is parallel to the polarization direction, in a similar manner to the schematics from Fig. 4.15 (b).

Figures 4.17 (b), (d) and (f) show the kinetic energy distribution for the  $S^+/S^{2+}$  coincidence channel as recorded after ionization with  $h\nu = 158$  eV,  $h\nu = 174$  eV and  $h\nu = 235$  eV photons, respectively. Using the mean KER from Fig. 4.17 of  $7.6 \pm 0.2$  eV and approximating the fragmentation process by a Coulomb explosion, one can calculate the mean charge separation distance in the parent ion before the dissociation by using Eq. 2.14.

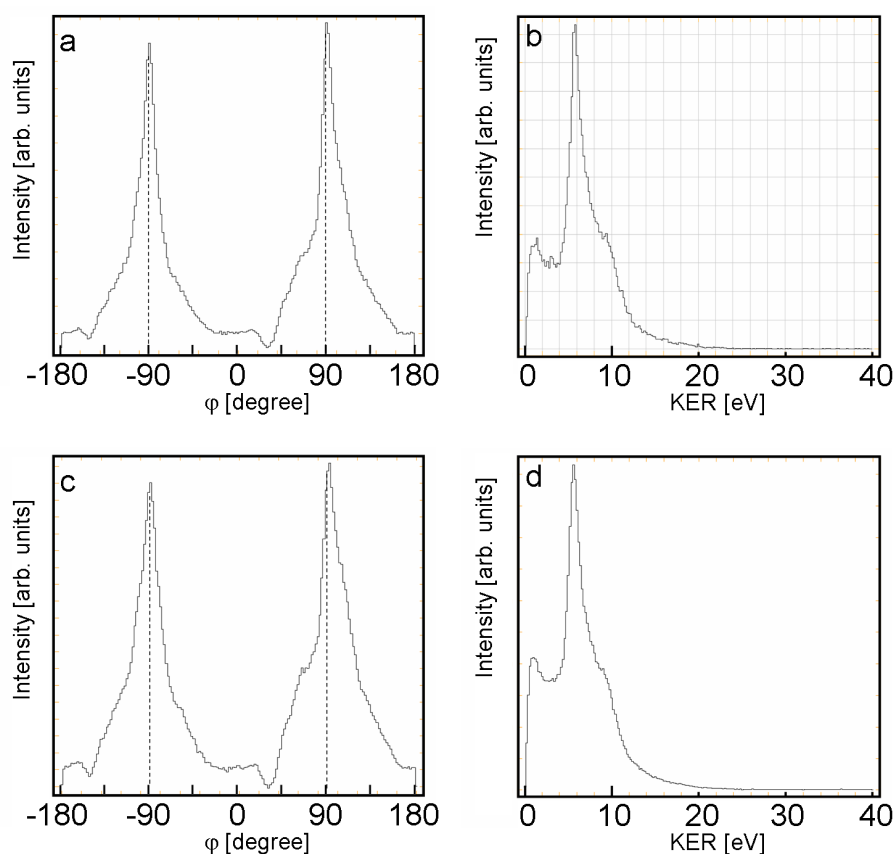


**Fig. 4.18:** KER distribution and KER distribution as a function of the  $\varphi$  angle for the  $S^+/S^+$  channel after ionization with  $h\nu = 174$  eV ((a) and(b)) and  $h\nu = 235$  eV ((c) and (d)) (see text for details)

Thus a mean charge separation distance of  $3.8 \pm 0.1 \text{ \AA}$  is obtained, which would indicate that the charges are located at second neighboring atoms in the parent ion, like atoms 1 and 3, with the notations from Fig. 4.7. In the previous work of Teodorescu *et al* [11], however, this coincidence channel has not been observed.

Figures 4.18 (a) and (c) present the kinetic energy distribution as a function of the angle between the emission direction of the particle and the direction of the synchrotron radiation,  $\varphi$  for the  $S^+/S^+$  cation pair. The excitation energies for the spectra in Fig. 4.18 (a) and (c) are  $h\nu = 174 \text{ eV}$  and  $h\nu = 235 \text{ eV}$ , respectively.

One observes that, similarly to the  $S^+/S^{2+}$  case, strong maxima are recorded for  $\pm 90^\circ$ , with minima at  $0^\circ$  and  $\pm 180^\circ$ . This fact indicates that the dissociation of sulfur aggregates takes place preferentially in the direction of the polarization of the ionizing synchrotron beam, and is inhibited for the direction perpendicular to it.

Figures 4.18 (b) and (d) presents the kinetic energy release distribution for the  $S^+/S^+$  ion-ion-coincidence channel as recorded after ionization at the  $h\nu = 174 \text{ eV}$  and  $h\nu = 235 \text{ eV}$  photon energy, respectively. Making use of the mean KER from Fig. 4.18, namely  $5.8 \pm 0.2 \text{ eV}$ , and Eq. 2.14, one can determine the mean charge separation distance as being  $2.5 \pm 0.1 \text{ \AA}$  for the break up into the  $S^+/S^+$  ion pair. Such a CSD means that the charges are located at adjacent sites in the doubly charged ion parent, e.g., using the notations from Fig. 4.7, atoms 1 and 2. The determined kinetic energy release is, however, slightly different from the reported value of Teodorescu *et. al.* [11], namely  $7.6 \pm 0.8 \text{ eV}$ . A possible reason for this difference could be the rather large size of the interaction region between the cluster beam and the synchrotron radiation.

Similarly to the  $S^+/S^{2+}$  case, an angular dependence of the kinetic energy release on the angle  $\varphi$  is observed (see Fig. 4.19 (a)) also for the  $S^{2+}/S^{2+}$  coincidence channel.

Figure 4.19 (b) depicts the kinetic energy distribution for the  $S^{2+}/S^{2+}$  coincidence channel, as recorded after ionization with  $h\nu = 235 \text{ eV}$ . As the photon energy is higher than the sulfur 2s edge ( $h\nu = 230 \text{ eV}$  [76]), a more intense signal for multiply charged sulfur ions is expected. The occurrence of the  $S^{2+}/S^{2+}$  coincidence channel appears to confirm this expectation, as it was not observed for the  $h\nu = 158 \text{ eV}$  and  $h\nu = 174 \text{ eV}$  (see Fig. 4.11).

From the mean value of the kinetic energy release (see Fig. 4.19 (b)) of  $7.0 \pm 0.2 \text{ eV}$  the charge separation distance in the parent ion was inferred to be  $8.2 \pm 0.2 \text{ \AA}$ . This is interpreted as a clear indication that in the parent ion the charges are located at opposite positions (e.g. atoms 1 and 5 in Fig. 4.7).

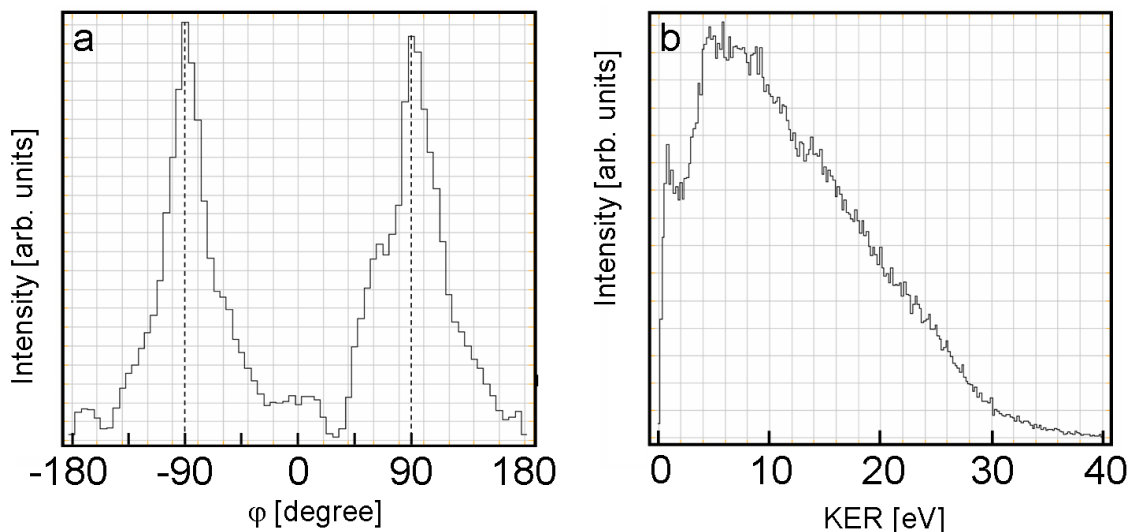


**Fig. 4.19:** KER distribution and KER distribution as a function of the  $\varphi$  angle for the  $S^{2+}/S^{2+}$  channel after ionization with  $h\nu = 235$  eV (see text for details)

### 4.2.3 Concluding Remarks

Photoelectron-photoion-photoion-coincidence experiments on sulfur clusters making use of a COLTRIMS setup have been for the first time successfully performed with synchrotron radiation at the sulfur 2p and 2s absorption edges.

From the analysis of the experimentally recorded data, the kinetic energy release distributions have been determined for all the coincidence channels observed ( $S^+/S^{2+}$ ,  $S^+/S^+$  and  $S^{2+}/S^{2+}$ ). From the calculated KER's, the charge separation distances have been inferred.

Kinetic energy distributions as a function of the  $\varphi$  angle exhibiting prominent maxima at  $\pm 90^\circ$  and minima at  $0^\circ$  and  $\pm 180^\circ$  have been observed for all sulfur ion pairs as well as for the  $N^+/N^+$  channel. Based on previous literature results [122, 123, 124, 125] this has been interpreted as an indication that the fragmentation of the aggregates takes place preferentially in the direction of the polarization of the synchrotron radiation.

## 4.3 Selenium Cluster Investigations

Selenium vapor is composed of a variety of clusters with sizes varying between 2 and 8 atoms, depending on the temperature [33][32]. The ionization energies for the different cluster sizes were determined previously via electron impact ionization measurements as being situated between 8.60 and 10.40 eV [33], as schematically depicted in Figure 4.9.

Cluster	Electron impact (eV)
$Se_2^+$	$9.2 \pm 0.1$
$Se_3^+$	$10.4 \pm 0.3$
$Se_4^+$	$10.1 \pm 0.3$
$Se_5^+$	$8.6 \pm 0.2$
$Se_6^+$	$8.8 \pm 0.2$
$Se_7^+$	$8.3 \pm 0.2$
$Se_8^+$	$9.3 \pm 0.2$

**Tab. 4.9:** Ionization potentials of selenium clusters represented as a function of the size of the cluster, as reported by Berkowitz [33]

In a similar manner to the sulfur case [11, 12], subsequent to core excitation various relaxation and fragmentation processes are expected to take place. It is most likely that the inner-shell excited ion will relax following Auger decay paths. This will lead to the occurrence of multiply charged aggregates.

The Auger decay of the core hole occurs on the femto- and picosecond time scale, which can be approximated as being instantaneous compared to the microsecond time scale of the flight-time of the ions in a mass spectrometer. Therefore it is expected that the final states detected using mass spectrometry techniques are multiply ionized [7]. It should also be not overlooked that Coulomb repulsion may contribute to the decay of multiply charged aggregates, leading most often to singly charged fragments.

In a similar manner to the investigations performed on sulfur cluster presented in Chapter 4.1., we have used the PEPIICO (Photoelectron-photoion-photoion-coincidence) technique to probe the fragmentation of selenium clusters after inner-shell excitation. This study is expected to help shed light on the dissociation paths of multiply charged selenium cations. We have performed PEPIICO experiments on selenium vapor kept at the constant temperature of 598 K using a photon energy  $h\nu = 150$  eV.

### 4.3.1 Mass Spectrometry

#### Mass spectrometry as a function of the temperature of the vapor

The mass spectra presented in Fig. 4.20 were recorded after ionization with radiation from a He I discharge lamp ( $h\nu = 21.22$  eV). As already mentioned shown in Tab.4.9, this energy is above the first ionization energy of selenium. The measurements were performed at two different temperatures, in order to evidence the occurrence of the selenium aggregates. However, due to

contamination of the sample with sulfur, the mass peaks marked with empty squares correspond to  $S_2^+$  (at  $4.8 \mu\text{s}$ ),  $S_4^+$  (at  $7.4 \mu\text{s}$ ) and  $S_6^+$  (at  $10.7 \mu\text{s}$ ).

The spectrum recorded at  $T = 297 \text{ K}$  is the mass spectrum of the residual gas at the pressure of  $2.1 \times 10^{-6} \text{ mbar}$ . The dominant peaks in the background spectrum (at  $2.2 \mu\text{s}$ ,  $2.5 \mu\text{s}$  and  $2.7 \mu\text{s}$ ) are the ones corresponding to  $m/q = 18$ ,  $m/q = 28$  and  $m/q = 32$  ( $(\text{H}_2\text{O})^+$ ,  $\text{N}_2^+$  and  $\text{O}_2^+$ , respectively, all components of the residual gas).

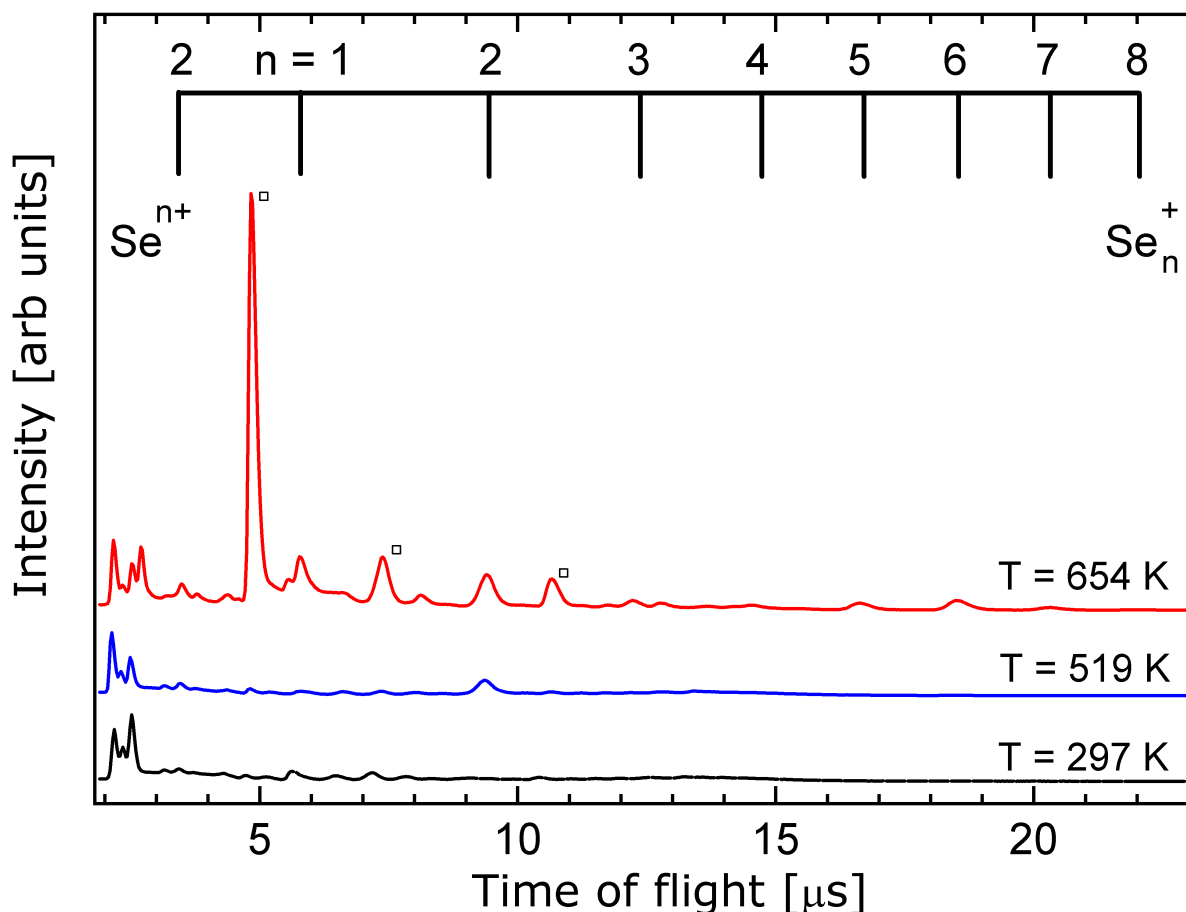


**Fig. 4.20:** Time of flight mass spectra of selenium clusters recorded after ionization with  $h\nu = 21.22 \text{ eV}$  photons

On increasing the temperature of the selenium vapor, the pressure in the experimental chamber increases reaching  $4.2 \times 10^{-6} \text{ mbar}$  at the temperature  $T = 544 \text{ K}$ . During the recording of this spectrum, the temperature of the first stage of the oven was kept constant at  $T = 544 \text{ K}$ , which is above the melting temperature of selenium ( $494 \text{ K}$ ). Important to notice is that at this temperature one can observe the occurrence of the peaks corresponding to  $m/q \approx 158$  (at  $9.4 \mu\text{s}$ ),  $m/q \approx 474$  (at  $18.5 \mu\text{s}$ ) and  $m/q \approx 553$  (at  $20.3 \mu\text{s}$ ) ( $\text{Se}_2^+$ ,  $\text{Se}_6^+$  and  $\text{Se}_7^+$  respectively).

It is worth reminding that selenium has 5 different isotopes with natural abundances higher than 7

%. These isotopes have masses between 76 amu and 82 amu (see Chapter 2.1.2 for more details), fact that can lead to a broadening of the peaks in the recorded mass spectra.

At  $T = 654$  K, an intense peak is recorded corresponding to  $m/q \approx 80$  ( $Se^+$ ). Apart from the monomer, one can also observe  $Se_2^+$ ,  $Se_3^+$ ,  $Se_4^+$ ,  $Se_5^+$ ,  $Se_6^+$ ,  $Se_7^+$  and even  $Se_8^+$ . As expected, the  $Se_8^+$  aggregate is fairly weak [33] whereas  $Se_6^+$  and  $Se_5^+$  are well visible.

Based on the earlier observations of Berkowitz and Chupka [32, 33], we can safely assume that the smaller clusters ( $Se_2^+$ ,  $Se_3^+$  and  $Se_4^+$ ) as well as atomic selenium are not produced as neutrals through the evaporation of solid selenium, but are rather the result of the fragmentation of larger Se clusters, such as  $Se_6^+$ .

The variation in the intensity of the selenium cluster species with temperature is summarized in Tab. 4.10. Table 4.10 presents the intensities of the mass peaks normalized to the intensity of the  $Se_2^+$  peak only for  $T = 519$  K and  $T = 654$  K, as for  $T = 297$  K no selenium cluster species are expected to occur.

Temperature [K]	$Se_8^+$	$Se_7^+$	$Se_6^+$	$Se_5^+$	$Se_4^+$	$Se_3^+$	$Se_2^+$	$Se^+$	$Se^{2+}$
519	-	0.07	0.11	-	-	-	1	-	-
654	0.05	0.12	0.33	0.25	0.24	0.28	1	1.59	0.52

**Tab. 4.10:** Mass peaks intensities normalized to the intensity of the  $Se_2^+$  mass peak, as recorded after ionization with  $h\nu = 21.2$  eV photons at different temperatures of selenium vapor, as shown in Fig. 4.20

## Mass spectrometry as a function of the ionization energy

Selenium clusters were also investigated in the inner-shell excitation regime. In order to be able to use for comparison the results obtained when using for ionization the He I discharge lamp radiation, the experiments were performed at  $T = 656$  K.

Mass spectra have been recorded for the ionization energies of 150 eV (in the  $Se-3d$  continuum), 1400 eV (below the  $Se - 2p$  edge) and 1450 eV (above the  $Se - 2p_{3/2}$  edge) and are presented in Fig. 4.21.

One observes that when the excitation energy is in the 3d-continuum ( $h\nu = 150$  eV) the most prominent mass peaks are the ones for the ratios  $m/q \approx 80$  and  $m/q \approx 40$ , which correspond to  $Se^+$  and  $Se^{2+}$ , respectively. It is also important to point out the peaks corresponding to  $N_2^+$  ( $m/q = 28$ ) and  $O_2^+$  ( $m/q = 32$ ), which are visible for flight times of  $2.1 \mu s$  and  $2.3 \mu s$ , respectively. These two peaks appear from the ionization of the background gas and were used for the mass calibration of the mass spectra recorded.

At the same time we note that also heavier selenium cations, like  $Se_2^+$  and  $Se_3^+$  are visible in this mass spectrum ( $m/q \approx 158$ ) and ( $m/q \approx 237$ ), respectively. Considering the earlier observations

of Berkowitz and Chupka with respect to the distribution of the neutrals in selenium vapor at the working temperature of 656 K, we can conclude that the singly charged cations observed are the result of fission of larger clusters [33].

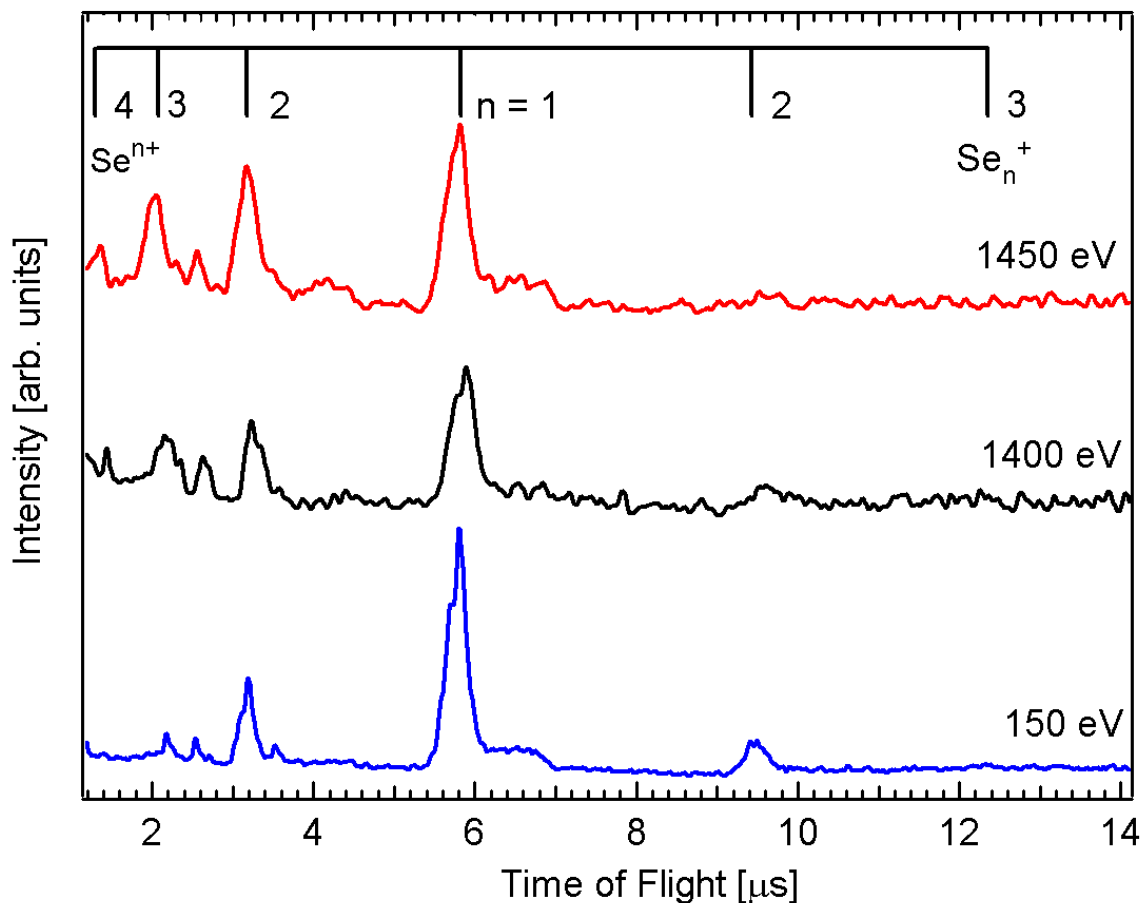


**Fig. 4.21:** Time of flight mass spectra of selenium clusters recorded at  $T = 656$  K after ionization with  $h\nu = 150$  eV and  $h\nu = 1450$  eV

When the excitation energy is  $h\nu = 1400$  eV (immediately below the Se 2p-edge), we observe that the singly charged selenium trimer is no longer visible. Also, the intensity of the peak corresponding to  $m/q = 158$  ( $Se_2^+$ ) has decreased, the peak being barely visible. At the same time, it is important to note that we observe two new peaks occurring at  $m/q \approx 26.33$  (at  $2.03 \mu s$ ) and  $m/q \approx 19.75$  (at  $1.35 \mu s$ ), as compared to the 3d-continuum excitation case. These peaks correspond to  $Se^{3+}$  and  $Se^{4+}$ , respectively. Responsible for the formation of the multiply charged selenium ions is assumed to be an Auger decay process of the *L-shell* excited selenium atom.

Upon the  $Se - 2p_{3/2}$  edge excitation ( $h\nu = 1450$  eV), the mass spectrum changes slightly. We observe that the intensity of the multiply charged ionic fragments increases. At the same time, we

note that neither the singly charged dimer nor the trimer are visible. We note that the selenium ion with the smallest  $m/q$  ratio recorded was  $Se^{4+}$  ( $m/q \approx 19.75$ ).

The variation in the intensity of the selenium cluster species with the ionization energy at constant selenium vapor temperature is summarized in Tab. 4.11. Table 4.11 presents the intensities of the mass peaks normalized to the intensity of the  $Se^+$  peak.

Ionization energy [eV]	$Se_3^+$	$Se_2^+$	$Se^+$	$Se^{2+}$	$Se^{3+}$	$Se^{4+}$
150	0.18	0.32	1	0.36	-	-
1400	-	-	1	0.74	0.59	0.27
1450	-	-	1	0.87	0.76	0.32

**Tab. 4.11:** Mass peaks' intensities normalized to the intensity of the  $Se^+$  mass peak, as recorded at  $T = 656$  K after ionization with various energy photons, as shown in Fig. 4.21

Based on the results presented in this section, one can conclude that increasing the temperature of selenium vapor, the occurrence ratio of the aggregates observed changes dramatically. At low temperature, 50 degrees above the melting temperature of selenium mainly  $Se_2^+$ ,  $Se_6^+$  and  $Se_7^+$  are observed. Increasing the temperature by 100 degrees, rather intense peaks corresponding to  $Se_3^+$ ,  $Se_4^+$  and  $Se_5^+$  have been noticed to occur. The largest aggregate observed was  $Se_8^+$ .

Investigating selenium clusters as a function of the ionization energy, it has been observed that for Se-3d excitation, mainly singly charged moieties are expected to occur. This in contrast to excitation by  $h\nu = 1450$  eV (above the Se-2p edge) where multiply charged selenium ions were observed, with no contribution from heavier aggregates.

### 4.3.2 PEPIICO Spectroscopy

Figure 4.22 presents the  $t_2$  vs  $t_1$  (where  $t_1$  is the arrival time of the first ion and  $t_2$  is the arrival time of the second ion) correlation plot of selenium cations recorded after inner shell ionization. This allows one to identify the resultant coincident fragmentation channels. The starting signals ( $t = 0$ ) are given by the electrons detected by the electron detector (see Chapter 3 for details). From the analysis of the shape and slope of the correlation plot  $t_2$  vs  $t_1$ , one can extract valuable information about the fragmentation dynamics of the process leading to this cation pair [60, 66, 112].

The experiments have been performed at the temperature  $T = 598$  K using soft x-rays with the photon energy  $h\nu = 150$  eV provided by the U49/2-PGM1 beam line of the BESSY II synchrotron radiation facility.

The identified coincidence channels from Fig. 4.22 are  $Se_2^+/Se_2^+$ ,  $Se^+/Se_2^+$ ,  $Se^+/Se^+$ ,  $Se^{2+}/Se^+$

and  $Se^{2+}/Se^{2+}$ . In the following section the coincidence signals as shown in Fig. 4.23) and analyzed and possible dissociation paths are proposed.

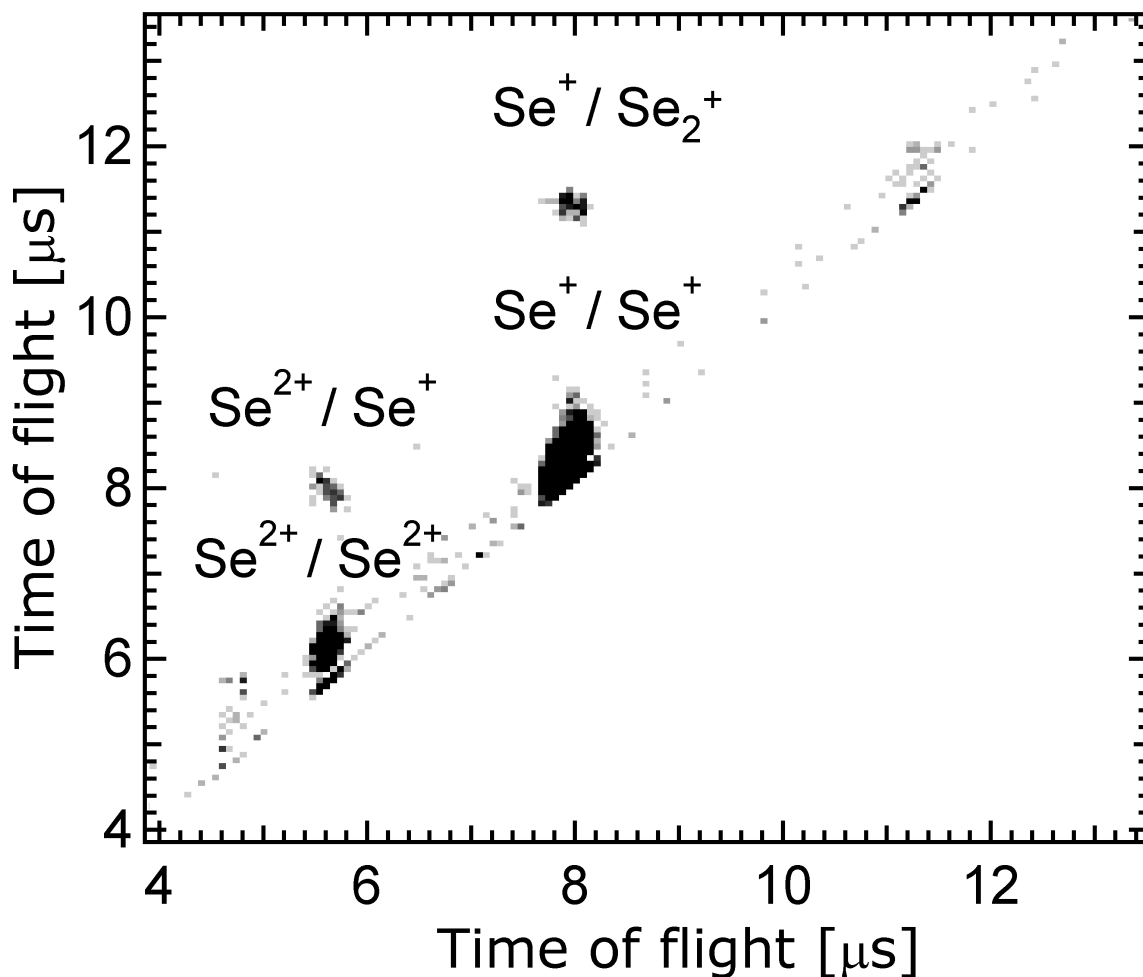


Fig. 4.22: PEPIICO spectrum of selenium clusters recorded after ionization with  $h\nu = 150$  eV

### $Se_2^{+}/Se^{+}$

The slope of the recorded  $Se_2^{+}/Se^{+}$  coincidence channel has been determined to be  $m = -0.6 \pm 0.6$ . This slope is interpreted as an evidence for a secondary decay process starting from  $Se_4^{2+}$ , as described by the following path:





However, the percentage of neutral  $Se_4$  is small in comparison to the amount of  $Se_5$  and  $Se_6$  [33]. Therefore it is considered safe to assume that  $Se_4^{2+}$  is the result of a decay of  $Se_5^{2+}$  or  $Se_6^{2+}$  via losses of neutrals.

The kinetic energy release accompanying the charge separation process is  $7.7 \pm 3.8$  eV, corresponding to a charge separation distance of  $1.9 \pm 0.6$  Å. This result is in agreement with earlier work [132] within experimental errors, indicating that the charges are located at neighboring atoms.

The release of the neutral in the second step of the decay is accompanied by a KER of  $10.5 \pm 3.0$  eV.

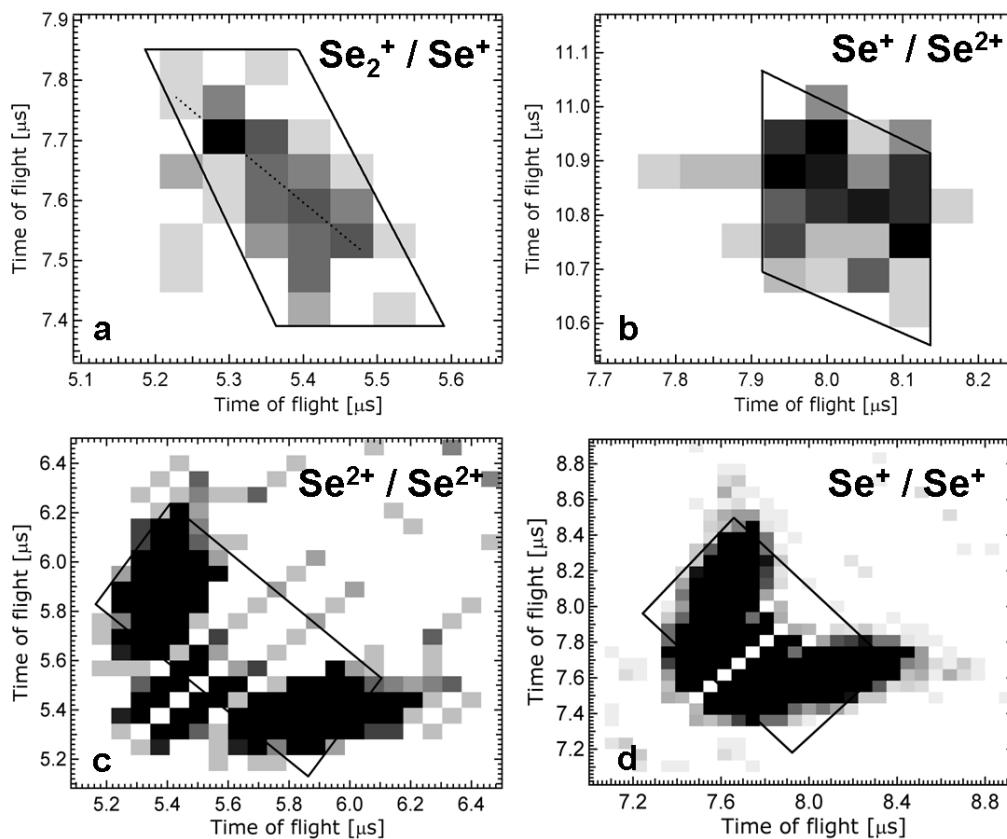


**Fig. 4.23:** Shapes of PEPICO signals from selenium ionic fragments resulting through ionization with  $h\nu = 150$  eV photons

### $Se^+ / Se^{2+}$

For the  $Se^+ / Se^{2+}$  coincidence channel a slope  $m = -1.7 \pm 0.7$  has been experimentally determined. A slope higher than -1 suggests a dissociation following a secondary decay path of the

lighter cation. However, no decay path was found that can explain the experimentally determined slope. Therefore, it has been concluded that the recorded coincidence signal occurs as a result of the superposition of two different processes, A and B.

Process A is a two-body dissociation of  $Se_2^{3+}$  as described by Eq. 4.25. This would lead to the occurrence of a coincidence island with a slope -1, which is depicted in Fig. 4.23 (b) by the dashed line:



Process B is a secondary decay process starting from  $Se_3^{3+}$  as described by Eq. 4.26. This would lead to a slope of the correlation plot of -2, suggested in Fig. 4.23 (b) by the parallelogram.



The kinetic energy releases corresponding to processes A and B are determined to be  $8.1 \pm 1.1$  eV and  $11.1 \pm 5.7$  eV, respectively. These correspond to charge separation distances of  $3.6 \pm 0.5$  Å and  $2.6 \pm 0.9$  Å, respectively. The release of neutral in the second step of process B is accompanied by a KER of  $9.2 \pm 5.1$  eV.

### **Se<sup>+</sup>/Se<sup>+</sup>**

The experimental slope for the  $Se^+/Se^+$  coincidence island was determined to be  $m = -1.1 \pm 0.2$ . This suggests a two-body dissociation mechanism starting from  $Se_2$ , as described by the mechanism:



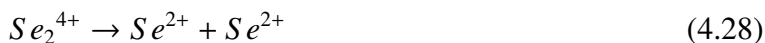
The KER for this process is  $19.2 \pm 3.3$  eV, which indicates a charge separation distance of  $0.8 \pm 0.2$  Å.

### **Se<sup>2+</sup>/Se<sup>2+</sup>**

For the  $Se^{2+}/Se^{2+}$  coincidence channel the experimental slope was determined to be  $m = -1.0 \pm 0.2$ . This is considered as a clear indication for a direct two body dissociation mechanism starting from  $Se_2^{4+}$ , as described by the following path:

Ion pair	Edge length (ns)	Edge slope	Proposed mechanism	KER (eV)	CSD (Å)
$Se_2^+/Se^+$	$255 \pm 77$	$m = -1.0 \pm 0.1$	$Se_4^{++} \rightarrow Se^+ + Se_3^+$	$7.7 \pm 3.8$	$1.9 \pm 0.6$
	$320 \pm 64$		$Se_3^+ \rightarrow Se_2^+ + Se$	$10.5 \pm 3.0$	
$Se^+/Se^{2+}$	$325 \pm 81$	$m = -1.0$	$Se_2^{3+} \rightarrow Se^{2+} + Se^+$	$8.1 \pm 1.1$	$3.6 \pm 0.5$
$Se^+/Se^{2+}$	$437 \pm 55$	$m = -2.0$	$Se_3^{3+} \rightarrow Se^{2+} + Se_2^+$	$11.1 \pm 5.7$	$2.6 \pm 0.9$
	$173 \pm 57$		$Se_2^+ \rightarrow Se^+ + Se$	$9.2 \pm 5.1$	
$Se^+/Se^+$	$996 \pm 91$	$m = -1.1 \pm 0.2$	$Se_2^{++} \rightarrow Se^+ + Se^+$	$19.2 \pm 3.3$	$0.8 \pm 0.2$
$Se^{2+}/Se^{2+}$	$905 \pm 91$	$m = -1.0 \pm 0.2$	$Se_2^{4+} \rightarrow Se^{++} + Se^{++}$	$15.9 \pm 3.3$	$3.6 \pm 0.6$

**Tab. 4.12:** Peak shape analysis of the ion-ion-coincidence signals shown in Fig.4.6.  $m$  represents the slope of the long edge of the correlation plots



However, considering the rather low concentration of neutral  $Se_2$  at the working temperature it is very likely that the  $Se_2^{4+}$  parent ion is the result of a decay of a larger selenium aggregate like  $Se_5$  and  $Se_6$ . Also, the possibility that this ion pair would occur in coincidence with another ion can not be completely discounted, as no quadruple coincidence measurements (PEPIPIICO) were performed.

The kinetic energy release accompanying the charge separation process was determined to be  $15.9 \pm 3.3$  eV, corresponding to a charge separation distance of  $3.6 \pm 0.6$  Å.

Table 4.12 summarizes the analysis of the coincidence correlation plots obtained subsequent to the ionization with  $h\nu = 150$  eV photons.

### 4.3.3 NEXAFS Spectroscopy

X-ray absorption studies provide important information on the occupied and unoccupied electronic states of substances [35, 133]. As it has been previously shown [134, 135, 136, 137, 138, 139, 140, 141, 142, 143] total electron yield detection methods have been successfully employed for the determination of x-ray absorption fine structures in experiments with small penetration depths.

For determining the selenium 2p near edge x-ray absorption fine structure in the gas phase, total electron yield and total ion yield spectra of selenium clusters have been recorded. The experiments have made use of synchrotron radiation provided by the BESSY U49/2-PGM-1 beam line. The experimental setup described in Chapter 3.3.1. was used for recording the data.

Earlier studies of Cardona *et. al.* [144] have shown that the Se-2p edge is expected to be seen in the energy interval 1400 – 1500 eV. In Fig. 4.24 the total ion yield (the blue curve) and the total electron yield (the red curve) spectra, together with the calculated data of Henke *et. al.* [145] for the energy interval between 1400 - 1500 eV are presented.

Distinct features are observed in this energy interval. However, the edge jump occurs at 1438.5 eV ( $2p_{3/2}$ ) and 1479.5 eV ( $2p_{1/2}$ ). These energies are slightly higher than the electron binding energies of elemental Se (1435.7 eV and 1476.4 eV) [145]. This indicates that there is a considerable chemical shift in clusters with respect to the single atom, in a similar manner to earlier reported results on aromatic clusters [146].

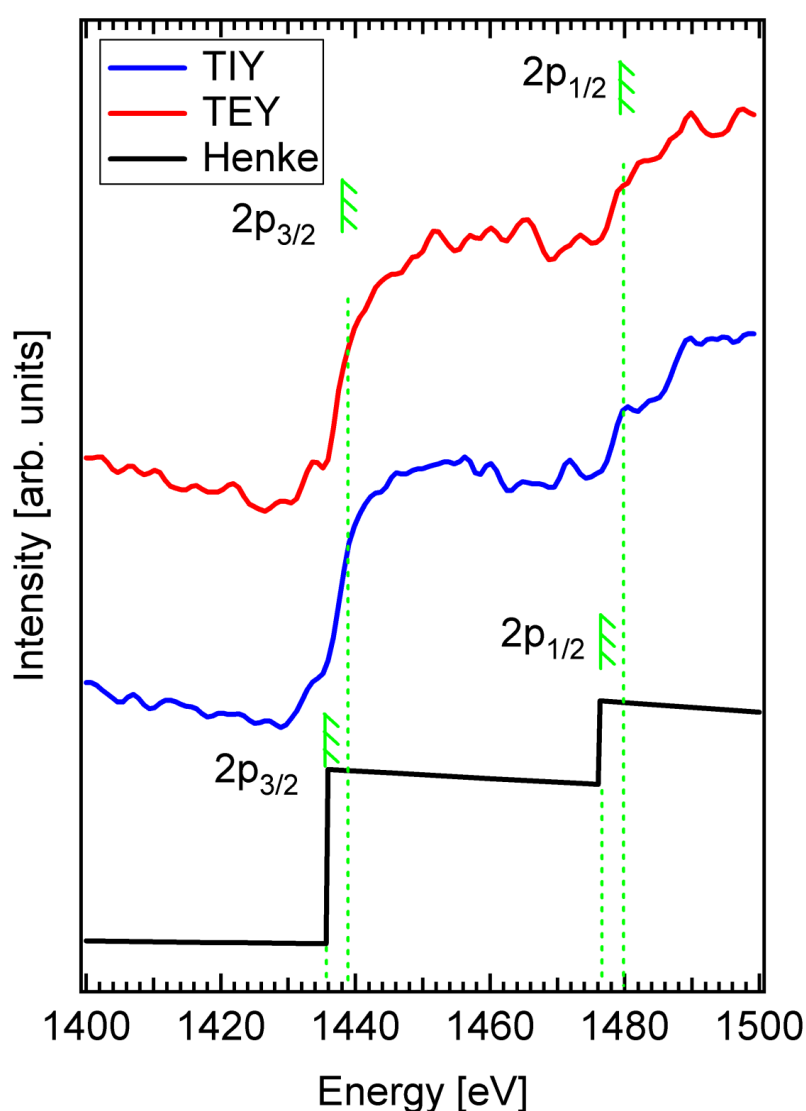


**Fig. 4.24:** Total yield spectra of selenium clusters recorded at the 2p-ionization edge

In the pre-edge regime one notices a broad resonant feature in the 1432 – 1436 eV energy range. Analogous to the previously reported data of Teodorescu *et. al.* [11] on sulfur clusters, this feature was attributed to transitions into unoccupied valence orbitals. However, for more insight, theoretical calculations are required.

For simulating the experimentally obtained NEXAFS spectra, the GSCF3 code [41, 42] was used. For an increased reliability of the theoretical results, a prior optimization of the geometrical structure of the  $Se_5$  and  $Se_6$  clusters was considered as being necessary.

The geometry of the  $Se_5$  and  $Se_6$  clusters was calculated using the Gaussian98 computing program [40]. The obtained results of the calculations are summarized in Tab. 4.13 and 4.14. The previously reported values of Miyamoto *et. al.* obtained from the refinement of the atomic parameters using the full matrix least squares method serve as a comparison for the present results on  $Se_6$ . For the optimization of the  $Se_5$  cluster geometry, the earlier reported results of Hohl *et. al.* were considered as a reference.

In Tab. 4.13 the following notations have been used:  $d_1 = d_{1,2} = d_{1,5}$ ,  $d_2 = d_{2,3} = d_{4,5}$ ,  $d_3 = d_{3,4}$ ,  $\alpha_1 = \angle 21 - 15$ ,  $\alpha_2 = \angle 12 - 23 = \angle 15 - 54$ ,  $\alpha_3 = \angle 23 - 34 = \angle 34 - 45$ ,  $\gamma_1 = \angle 21 - 54$ ,  $\gamma_2 = \angle 12 - 34$

Figure 4.25 (a) and (b) presents the geometries of the  $Se_5$  (a) and  $Se_6$  (b) clusters as inferred from the geometry optimization calculations. For the  $Se_5$  and  $Se_6$  aggregates, the bond lengths are 2.5407 Å and 2.4812 Å, with the bond angles ( $\alpha$ ) 3-2-1 of 89.57° and 100.50° while the dihedral angles ( $\gamma$ ) 4-3-2-1 are determined to be -64.52° and 133.96°, respectively.

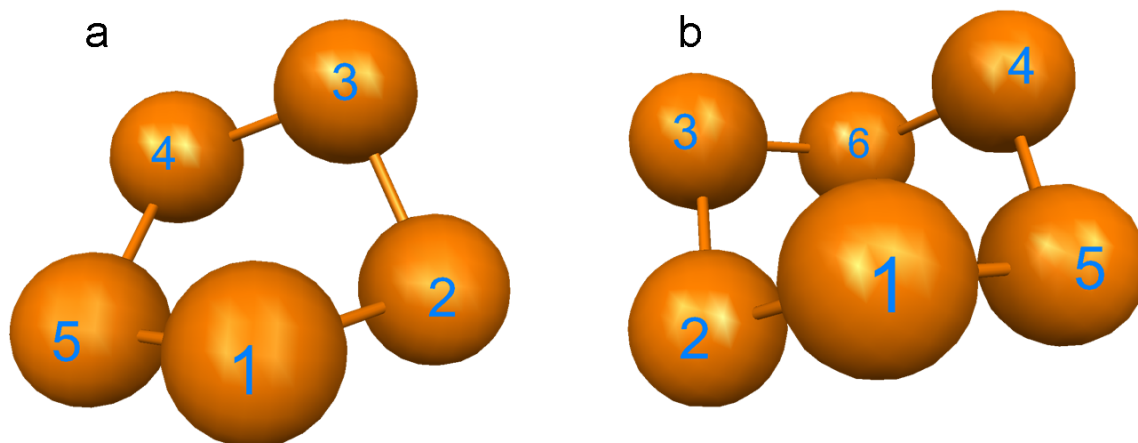


**Fig. 4.25:** The structure of the  $Se_5$  (a) and  $Se_6$  (b) clusters used for the simulations performed using the GSCF3 code

For the calculations performed with the GSCF3 code, the geometries presented in Fig. 4.25 were

employed. Also, the basis set proposed by Huzinaga [147] was considered. For the theoretical results, the composition of the selenium vapor was assumed based on the earlier reported results of Berkowitz *et. al* [33]. The calculations were performed independently for the two selenium species, and the results were afterwards added in the correct ratios.

The theoretical spectrum obtained is presented in Fig. 4.26. The upper curve presents the experimentally recorded total electron yield spectrum for the energy interval 1424 – 1438 eV. The presented experimental spectrum was recorded with 512 points and was normalized to the photon flux of the beam line.

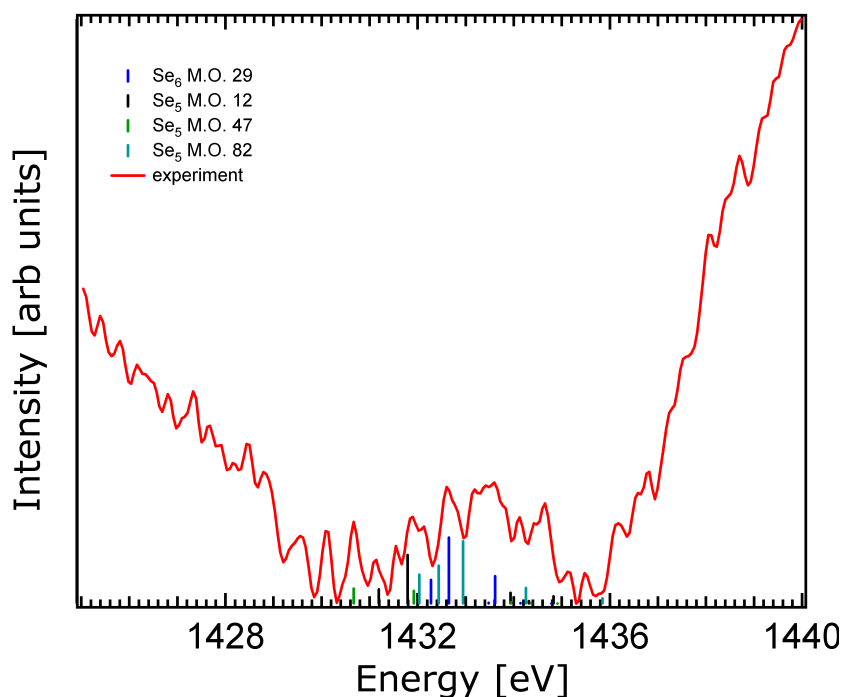


**Fig. 4.26:** Total electron yield of the near-edge structure of selenium clusters recorded at the 2p-ionization edge

Calculations have been performed for all selenium atoms and for both geometries. However, for the  $Se_6$  cluster, the selenium atoms are equivalent, such that presenting the results of the simulation for the hole located at only one of the atoms will suffice. The results of the calculations for  $Se_6$  for the core hole located at atom 1 (molecular orbital (m. o.) 29) with the GSCF3 code are summarized in Tab. 4.15.

For the  $Se_5$  aggregate, however, as the atoms are not equivalent, as it was also shown by the geometry optimization results. Therefore for  $Se_5$  Tab. 4.15 presents the results for three different localizations of the core hole, namely at orbitals 12, 47 and 82.

From the theoretical results presented in Tab. 4.15 one can conclude that, in what concerns the  $Se_5$  cluster excited at M. O. 12, the two most intense transitions have most of their character from the atoms located the furthest away from the excited atom (atoms 3 and 4, as denoted in Fig. 4.25 (a)). The least intense transitions are to molecular orbitals involving mostly the excited atom and the two adjacent atoms (atoms 1, 2 and 5, with the notations from Fig. 4.25 (a)).

For the localization of the core hole at M. O. 47 and 82 one can conclude that the most intense transitions are to molecular orbitals involving atoms 4, 5 and 1 and 2,5 and 3, respectively. The least intense transitions appear to be to molecular orbitals involving the excited atom and the neighboring atoms (3,2 and 1 and 2,3 and 4, respectively).

For the  $Se_6$  aggregate, however, the most intense transitions are to molecular orbitals that involve mostly the core excited atom and the two neighboring atoms (atoms 1, 2 and 5, with the notations from Fig. 4.25 (b)). The least intense transitions observed for the  $Se_6$  cluster are to molecular orbitals which have less character from the core excited atom and are located at the opposite end of the cluster (atoms 3, 6 and 4, with the notations from Fig. 4.25 (b)). Being located at the other end of the cluster, it is to be expected that they have the least overlap with the core excited atom, which would explain their weak oscillator strength.

#### 4.3.4 Concluding remarks

Investigations of selenium clusters as a function of the temperature and in the Se-2p regime have been performed. Varying the temperature at constant ionization energy ( $h\nu = 21.22 eV$ ), it has been noticed that the ratios of the heavier aggregates decreases while the intensity of the smaller clusters increases.

The presented data on the inner shell excitation of selenium clusters indicate that upon Se-2p ionization multiply charged selenium moieties occur (up to  $Se^{4+}$ ). However, there is no evidence for singly charged heavier aggregates (such as  $Se_3^+$ ), as observed for Se-3d continuum ionization.

PEPIPICO spectroscopy investigations have been also performed on the fragmentation of selenium clusters subsequent to ionization by  $h\nu = 150 eV$  photons. The analysis of the experimental data has lead to the identification of several coincidence channels, and possible fragmentation paths have been proposed.

Total electron and total ion yields of selenium in the gas phase have been for the first time recorded around the Se-2p absorption edge. The broad resonant feature observed in the 1428 - 1435 eV energy range has been assigned to the transitions into unoccupied molecular orbitals. This assignment was supported by theoretical calculations with the GSCF3 code.

Basis set	Bond length [ $\text{\AA}$ ]	$\alpha$ [ $^\circ$ ]	$\gamma$ [ $^\circ$ ]
<i>HF/STO-3G</i>	$d_1 = 2.343 \pm 0.0001$ $d_2 = 2.3554 \pm 0.0005$ $d_3 = 2.3859 \pm 0.0003$	$\alpha_1 = 94.155 \pm 0.0000$ $\alpha_2 = 98.1601 \pm 0.05$ $\alpha_3 = 102.8383 \pm 0.024$	$\gamma_1 = 61.0608 \pm 0.1148$ $\gamma_2 = 37.5609 \pm 0.2946$
<i>HF/3-21G</i>	$d_1 = 2.4745 \pm 0.0000$ $d_2 = 2.4860 \pm 0.0000$ $d_3 = 2.5372 \pm 0.0000$	$\alpha_1 = 92.9239 \pm 0.0000$ $\alpha_2 = 97.8796 \pm 0.0088$ $\alpha_3 = 102.1980 \pm 0.0025$	$\gamma_1 = 62.9308 \pm 0.0160$ $\gamma_2 = 38.8454 \pm 0.0410$
<i>HF/6-31G</i>	$d_1 = 2.4267 \pm 0.0000$ $d_2 = 2.4373 \pm 0.0002$ $d_3 = 2.5048 \pm 0.0000$	$\alpha_1 = 89.9575 \pm 0.0000$ $\alpha_2 = 96.1361 \pm 0.0303$ $\alpha_3 = 100.9526 \pm 0.0068$	$\gamma_1 = 67.8649 \pm 0.0525$ $\gamma_2 = 41.7894 \pm 0.1330$
<i>HF/6-311G</i>	$d_1 = 2.4641 \pm 0.0001$ $d_2 = 2.4545 \pm 0.0000$ $d_3 = 2.5574 \pm 0.0000$	$\alpha_1 = 92.1808 \pm 0.0000$ $\alpha_2 = 98.7829 \pm 0.0175$ $\alpha_3 = 101.6724 \pm 0.0021$	$\gamma_1 = 62.8745 \pm 0.0152$ $\gamma_2 = 39.0974 \pm 0.0480$
<i>MP2/STO-3G</i>	$d_1 = 2.3732 \pm 0.0001$ $d_2 = 2.3836 \pm 0.0002$ $d_3 = 2.4255 \pm 0.0000$	$\alpha_1 = 93.4324 \pm 0.0000$ $\alpha_2 = 97.9617 \pm 0.0405$ $\alpha_3 = 102.4815 \pm 0.0131$	$\gamma_1 = 62.2490 \pm 0.0784$ $\gamma_2 = 38.3036 \pm 0.2005$
<i>MP2/3-21G</i>	$d_1 = 2.522 \pm 0.0001$ $d_2 = 2.5173 \pm 0.0003$ $d_3 = 2.6074 \pm 0.0000$	$\alpha_1 = 91.2329 \pm 0.0000$ $\alpha_2 = 98.2003 \pm 0.0088$ $\alpha_3 = 101.4226 \pm 0.0113$	$\gamma_1 = 62.3247 \pm 0.0117$ $\gamma_2 = 40.0090 \pm 0.0311$
<i>MP2/6-31G</i>	$d_1 = 2.4808 \pm 0.0000$ $d_2 = 2.4662 \pm 0.0001$ $d_3 = 2.5874 \pm 0.0000$	$\alpha_1 = 87.6846 \pm 0.0000$ $\alpha_2 = 96.4977 \pm 0.0010$ $\alpha_3 = 99.9173 \pm 0.0002$	$\gamma_1 = 69.5224 \pm 0.0057$ $\gamma_2 = 43.3203 \pm 0.0233$
<i>MP2/6-311G</i>	$d_1 = 2.4641 \pm 0.0001$ $d_2 = 2.4545 \pm 0.0000$ $d_3 = 2.5574 \pm 0.0000$	$\alpha_1 = 92.1808 \pm 0.0000$ $\alpha_2 = 98.7829 \pm 0.0175$ $\alpha_3 = 101.6724 \pm 0.0021$	$\gamma_1 = 62.8745 \pm 0.0152$ $\gamma_2 = 39.0974 \pm 0.0480$
<i>B3PW91/LANL2DZ</i>	$d_1 = 2.5216 \pm 0.0001$ $d_2 = 2.4664 \pm 0.0001$ $d_3 = 2.6133 \pm 0.0000$	$\alpha_1 = 89.2265 \pm 0.0000$ $\alpha_2 = 98.9794 \pm 0.0093$ $\alpha_3 = 100.8502 \pm 0.0020$	$\gamma_1 = 62.8745 \pm 0.0152$ $\gamma_2 = 41.0446 \pm 0.0144$
<i>B3LYP/LANL2DZ</i>	$d_1 = 2.5407 \pm 0.0003$ $d_2 = 2.4854 \pm 0.0000$ $d_3 = 2.6335 \pm 0.0000$	$\alpha_1 = 89.5682 \pm 0.0000$ $\alpha_2 = 99.0894 \pm 0.0300$ $\alpha_3 = 100.9688 \pm 0.0115$	$\gamma_1 = 64.5309 \pm 0.0142$ $\gamma_2 = 40.7160 \pm 0.0572$
reference [132]	$d_1 = 2.4562$ $d_2 = 2.3685$ $d_3 = 2.5494$	$\alpha_1 = 87$ $\alpha_2 = 100$ $\alpha_3 = 100$	$\gamma_1 = 66$ $\gamma_2 = 42$

**Tab. 4.13:** Geometry optimization results as obtained from using the Gaussian98 [40] program, with different basis sets

Cluster size	Basis set	Bond length [ $\text{\AA}$ ]	$\alpha$ [ $^\circ$ ]	$\gamma$ [ $^\circ$ ]
$Se_6$	<i>HF/STO-3G</i>	$2.3496 \pm 0.0001$	$100.5621 \pm 0.0021$	$77.0341 \pm 0.0011$
$Se_6$	<i>HF/3-21G</i>	$2.5265 \pm 0.0001$	$100.6889 \pm 0.0001$	$76.8376 \pm 0.0003$
$Se_6$	<i>HF/6-31G</i>	$2.4255 \pm 0.0001$	$97.2699 \pm 0.0003$	$81.7604 \pm 0.0013$
$Se_6$	<i>HF/6-311G</i>	$2.4183 \pm 0.0001$	$101.9241 \pm 0.0001$	$74.9051 \pm 0.0006$
$Se_6$	<i>MP2/STO-3G</i>	$2.3803 \pm 0.0001$	$100.4081 \pm 0.0013$	$77.2643 \pm 0.0040$
$Se_6$	<i>MP2/3-21G</i>	$2.5265 \pm 0.0001$	$100.6889 \pm 0.0003$	$76.8380 \pm 0.0009$
$Se_6$	<i>MP2/6-31G</i>	$2.4750 \pm 0.0001$	$96.9699 \pm 0.0003$	$82.0619 \pm 0.0006$
$Se_6$	<i>MP2/6-311G</i>	$2.4666 \pm 0.0001$	$101.6556 \pm 0.0005$	$75.3360 \pm 0.0029$
$Se_6$	<i>B3PW91/LANL2DZ</i>	$2.5068 \pm 0.0001$	$101.0821 \pm 0.0055$	$76.2355 \pm 0.0040$
$Se_6$	<i>B3LYP/LANL2DZ</i>	$2.5257 \pm 0.0001$	$101.3151 \pm 0.0077$	$76.2355 \pm 0.0060$
$Se_6$	reference [148]	$2.356 \pm 0.009$	$101.1 \pm 0.3$	$76.2 \pm 0.4$

**Tab. 4.14:** Geometry optimization results as obtained from using the Gaussian98 [40] program, with different basis sets

Cluster size	Excited M. O.	Molecular orbital	Term value [eV / n*]	Oscillator strength
$Se_5$	12	86	-7.308 / 1.36	0.0001612
$Se_5$	12	87	-6.709 / 1.42	0.0005464
$Se_5$	12	88	-4.568 / 1.73	0.0001226
$Se_5$	12	89	-4.184 / 1.80	0.0000291
$Se_5$	12	90	-3.672 / 1.92	0.0000833
$Se_5$	47	86	-7.830 / 1.32	0.0169569
$Se_5$	47	87	-6.581 / 1.44	0.0143825
$Se_5$	47	88	-4.559 / 1.73	0.0016189
$Se_5$	47	89	-4.139 / 1.81	0.0005179
$Se_5$	47	90	-3.590 / 1.95	0.0002299
$Se_5$	82	88	-6.464 / 1.45	0.3245426
$Se_5$	82	89	-6.061 / 1.50	0.4249825
$Se_5$	82	90	-5.556 / 1.56	0.6977251
$Se_5$	82	86	-4.249 / 1.79	0.1764960
$Se_5$	82	87	-2.653 / 2.26	0.0598530
$Se_6$	29	107	-6.224 / 1.48	0.0002680
$Se_6$	29	108	-5.851 / 1.52	0.0007409
$Se_6$	29	103	-5.023 / 1.65	0.0000101
$Se_6$	29	104	-4.887 / 1.67	0.0003092
$Se_6$	29	105	-4.361 / 1.77	0.0000071
$Se_6$	29	106	-3.717 / 1.91	0.0000023

**Tab. 4.15:** Theoretical results obtained with the GSCF3 code for the  $Se_5$  and  $Se_6$  aggregates

